CHALMERS
UNIVERSITY OF TECHNOLOGY

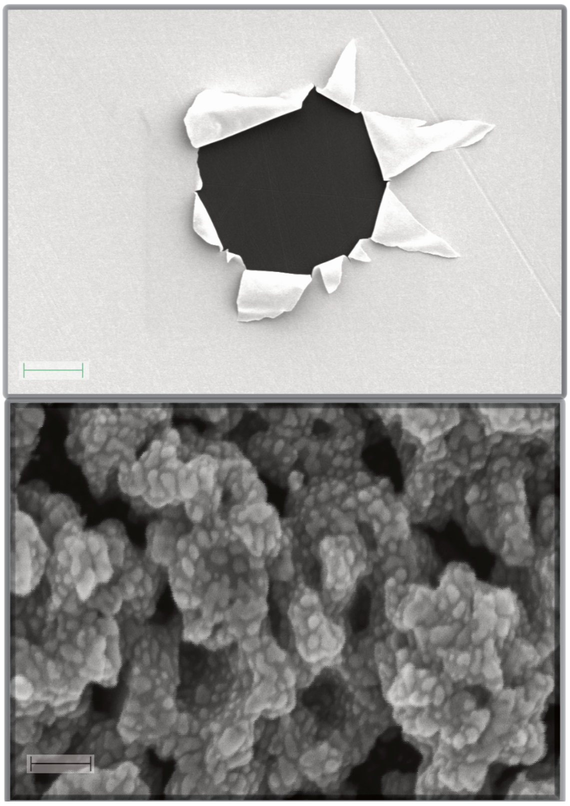

W_xC thin films supports for Cathode Catalysts in Anion Exchange Membrane Fuel Cells

Investigating the effects of using tungsten carbide as catalyst support in order to boost specific activity of the catalyst

Master's thesis in Physics

Elias Elmquist

DEPARTMENT OF PHYSICS
CHALMERS UNIVERSITY OF TECHNOLOGY
Gothenburg, Sweden 2022
www.chalmers.se

MASTER'S THESIS 2022

W_xC thin film supports for cathode catalysts in Anion Exchange Membrane Fuel Cells

Investigating the effect of using tungsten carbide as catalyst support in order to boost specific activity of the electrocatalyst

ELIAS ELMQUIST

Department of physics
Division of Chemical Physics
Group of Björn Wickman
CHALMERS UNIVERSITY OF TECHNOLOGY
Gothenburg, Sweden 2022

W_xC thin film supports for cathode catalysts in Anion exchange membrane fuel cells
Investigating the effects of using tungsten carbide as catalyst support in order to boost specific activity of the electrocatalyst
Elias Elmquist

Supervisor: Gerard Montserrat Siso, Chemical Physics
Examiner: Björn Wickman, Chemical Physics

Master's Thesis 2022
Department of Physics
Division of Chemical Physics
Group of Björn Wickman
Chalmers University of Technology
SE-412 96 Gothenburg
Telephone +46 31 772 1000

Cover: (Left) Sputtering W_xC, Argon plasma at the top and rays of W_xC are going downwards. (Top right) hole in W_xC layer, scalebar 20 μm (bottom right) Ag nano agglomerates on W_xC substrate, scalebar 100 nm. Photographed using SEM.

Typeset in LaTeX
Printed by Chalmers Reproservice
Gothenburg, Sweden 2022
'This work was performed in part at Myfab Chalmers.'

W_xC thin film supports for cathode catalysts in Anion exchange membrane fuel cells
Investigating the effects of using tungsten carbide as catalyst support in order to boost specific activity of the catalyst
Elias Elmquist
Department of Chemical Physics
Chalmers University of Technology

Abstract

The prospect of a CO_2 emission free hydrogen energy system requires the development of effective and inexpensive fuel cell catalysts from abundant resources. One promising path forward is the development of anion exchange membrane fuel cells (AEMFC). Thanks to their alkaline environment, they are more flexible regarding catalyst material, thus potentially reducing their cost compared to current fuel cell technology.

In this study, W_xC thin films are evaluated as support for different catalytic materials with the aim to reduce catalyst loading and increase specific current density. Using sputtering and physical vapour deposition, thin films with high uniformity and high control over composition can be fabricated. Through rotating disk electrode techniques, the oxygen reduction reaction activity of these thin film electrocatysts is measured in alkaline media. Tested catalystic thin films are Pt, Pd, Cu and Ag. Pt and Pd show good onset potential and an improved mass activity compared to Pt. Cu and Ag evaporated on W_xC exhibit less ORR activity in alkaline media. The results also indicate that W_xC improves the stability of very thin Pt layers with respect to cycle-life compared to Pt. This suggests a possible further reduction of catalytic material is on the horizon.

Keywords: Anion exchange membrane fuel cells, AEMFC, Tungsten carbide, W_xC

Acknowledgements

I would like to thank for my supervisor Gerard, for his great patience in teaching me electrochemistry and guiding me forward. I have especially appreciated to have someone to direct all my questions to who always has taken their time to answer any questions I have had. The combination of trust in my ability and guidance has been great! It has been a great learning experience and I have really appreciated being able to try out all the interesting techniques used in this masters thesis.
I would also like to thank Mathilde, Björn, Roopathy, Victor and the rest of the group for their support and having made this thesis a fun experience. Also I would like to thank Björn for giving me this opportunity!

Finally, this work would not have been possible without the possibility of working in the clean room environment at Myfab Chalmers.

Elias Elmquist, Gothenburg, May 2022

List of Acronyms

Below is the list of acronyms that have been used throughout this thesis listed in alphabetical order:

AEM	Anion exchange membrane
CV	cyclic voltammetry
ECSA	Electrochemical surface area
EIS	Electrochemical impedance spectroscopy
*FC	* Fuel cell
GC	Glassy carbon
HER	Hydrogen evolution reaction
HOR	Hydrogen oxidation reaction
IR	Internal resistance
KL	Koutecký-Levich
MEA	Membrane electrode assembly
MT	Mass transport
ORR	Oxygen reduction reaction
PEM	Proton exchange membrane
RDE	Rotating disk electrode
RHE	Reversible hydrogen electrode
RRDE	Rotating ring disk electrode

Nomenclature

Below is the nomenclature of indices, sets, parameters, and variables that have been used throughout this thesis.

Electrochemical parameters

i	Current $[A]$
j	Current density $[A/cm]$
E	Electric potential difference $[V]$
η_{cell}	Fuel cell efficiency [ ]
ϕ	Electric field potential $[V]$
μ_j	chemical potential of j $[eV]$
Z_j	Charge of species j $[C]$
c_j	Concentration of j $[mol/l]$
C	Capacitance $[F]$
E^0	Electromotive force (potential of cell) $[V]$
η	Overpotential of a fuel cell $[V]$
β	Assymetry parameter in chemical reacion [ ]
k, k^+, k^-	Reaction rates, anodic and cathodic direction $[mol/ls]$

Electrocatalysis parameters

E_o	Electric onset potential $[V]$
$E_{1/2}$	Half-wave potential $[V]$
$ECSA_{cap}$	Electrochemical active surface area from surface capacitance $[cm^2]$
$ECSA_{HUPD}$	Electrochemical active surface area form hydrogen underpotential deposition $[cm^2]$
n_e	Electron transfer coefficient in reaction eg. ORR [ ]
i_k	Limiting kinetic current $[A]$

Contents

List of Figures

List of Tables

1

Introduction

1.1 H_2 in a sustainable energy system

The transition towards emission free energy systems has come a long way. Electrification has come a long way in many sectors with widespread use of electric cars, bikes and others. However, for many applications today the battery electric solution does not seem a viable alternative[1]. For these applications often the amount of on board energy storage, or the time the energy needs to be stored for means that the battery electric alternative is not up to the challenge. For these applications, fuel cells (FC) offer a way to de-carbonise sectors which previously have not been able to be de-carbonised. Examples of such sectors are heavy transport (long haul trucks, boats, medium range flight etc.) and mid to long term energy storage where storage of energy as H_2 is a way to counteract seasonal changes in electricity production. In a FC H_2 and O_2 are combined to form H_2O and electric current without any direct green house gas emissions.

Possible application of FCs are plentiful with it being able to replace most large scale battery storage's. In a scenario where FC are widely implemented, however, a very large portion of the production cost would come from the catalyst raw material with today's technology. Therefore it is necessary to further improve the FC catalyst.

1.1.1 Fuel cell system layout

A fuel cell system in any application will consist of a large set of components including fuel storage, balance of plant components (cooling, pumps, filters etc) and at the heart of it the fuel cell stack. The basic layout of a fuel cell stack is a series of n individual FC connected in series, each one comprised of bipolar plates on either sides and in the center the membrane electrode assembly (MEA), as illustrated in the fig. 1.1. The bipolar plates and the gas diffusion layer (GDL) serve as electrical connectors from cell to cell, all whilst allowing gases to have access to the catalyst layers. The catalyst is where the electrochemical reactions take place. This is where oxygen and hydrogen react to form water with electricity as a product.

The electricity generated by the FC is generated in the form of potential across the cell. A normal operating potential for a low temperature FC is around 0.7 V [2, ch 1.3], this is too low to be useful for most applications and therefore many cells are connected in series to form a FC stack. This gives the total operating voltage of the stack as $V_{stack} = V_{cell} * n_{cells}$ where V_{cells} is the potential of one cell and n_{cells} is the number of cells in the stack.

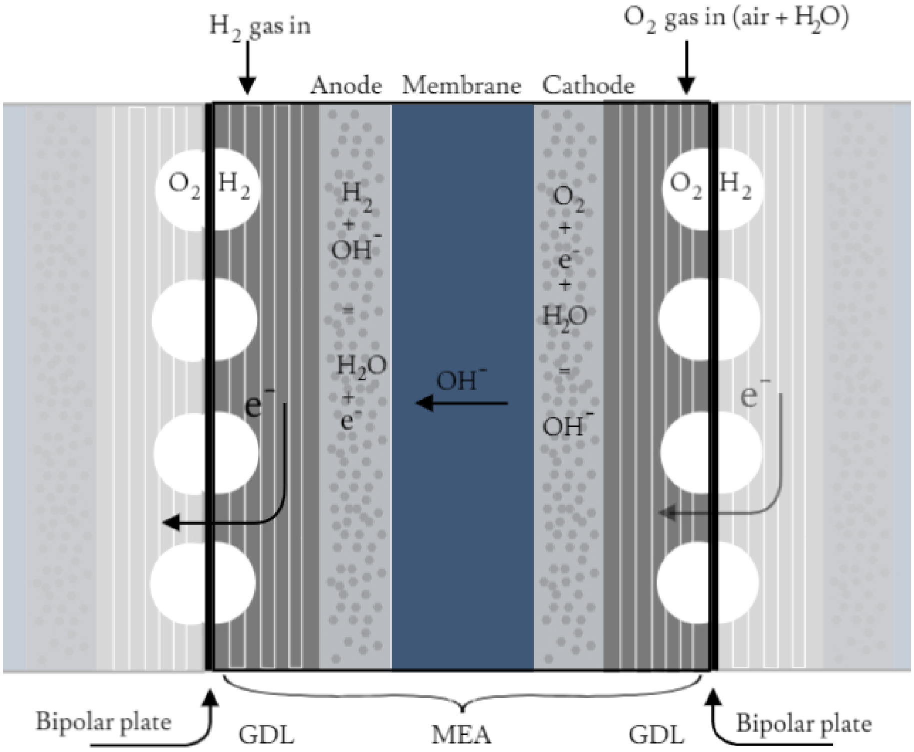

Figure 1.1: Sketch of the cross section of an anion exchange membrane fuel cell, on the sides are the greyed out parts of the previous and next cell in the stack. Marked in the sketch is the bipolar plates, the membrane electrode assembly (MEA) with subcomponents as the gas diffusion layer (GDL). Inside the MEA the reactions taking place on the catalysts are noted.

1.1.2 Fuel cell types

Many different variants of FCs exist, these are usually classified depending on what material is used in the membrane of the MEA. The conditions inside the membrane dictates the conditions for operation which justifies this as the main focus of classification. The two mayor types are low temperature fuel cell, from which the proton exchange membrane (PEM) FCs is the most common of all and high temperature (HT) FCs. Their operating conditions vary wildly, with the membrane in the HTFC operating at 800 °C where as the PEM operates as < 100 °C. This work will focus entirely on, anion exchange membrane fuel cell (AEMFC), a type of low temperature FC. It shares many systemic similarities with the PEMFC and uses a polymeric membrane but operates in an alkaline environment instead of a acidic one.

1.2 Anion exchange membrane fuel cells

The main system feature that defines an AEMFC is the alkaline environment in the electrolyte. This means the membrane conducts OH^--groups while hindering all other species from passing through. The overall reaction in the FC is the same as for a it's acidic analog PEMFC however namely $H_2 + O_2 \longrightarrow H_2O$. This can be divided into the reactions happening on the different sides of the membrane, on the anode side the hydrogen oxidation reaction (HOR) is taking place, which can be written

$$2H_2 + 4OH^- \rightarrow 4H_2O + 4e^- \tag{1.1}$$

and on the cathode side the oxygen reduction reaction (ORR) is taking place, this reaction has two main pathways which it can follow, the 4e pathway or the 2e pathway. The 4e pathway is as follows

$$\mathrm{O_2 + 2\,H_2O + 4\,e^- \longrightarrow 4\,OH^-} \tag{1.2}$$

and the 2 electron pathway [3]

$$O_2 + H_2O + 2e^- \rightarrow HO_2^- + OH^- \tag{1.3}$$

$$HO_2^- + H_2O + 2e^- \rightarrow 3OH^- \tag{1.4}$$

Hydrogen peroxide $\mathrm{HO_2}^-$ is a powerful oxidiser and is suspected to have a large role in the FC membrane degeneration [4], [5] therefore the 4 electron pathway is preferred.

1.2.1 AEMFC efficiency and power

The standard way to characterize a FC is through a Current-Voltage curve or polarisation curve, and example of such a curve can be seem in fig. 1.2. This shows the operating voltage at different current outputs. The total power output P_{cell} of the FC can be calculated as

$$P_{cell} = U_{cell} * I_{cell}. \tag{1.5}$$

The maximum voltage that can be achieved in a FC is given by the Gibbs free energy released per mol of reactant as $U_{ideal} = \frac{237}{2F}\frac{[KJ/mol]}{[C/mol]} = 1.23$ V with the 2 stemming from two electrons being released per mol of reaction, F being Faradays constant[2, eq. 2.1]. This is called the ideal reversible voltage of the cell. The maximum energy put in the system however is the enthalpy change and can be calculated as $U_{\eta 100} = \frac{286}{2F}\frac{[KJ/mol]}{[C/mol]} = 1.48$ V. Through this the efficiency of the FC can be calculated as

$$\eta_{cell} = \frac{U_{cell}}{1.48} * 100 \quad [\%] \tag{1.6}$$

The maximum FC efficiency can therefore easily be calculated as $\frac{1.23}{1.48} * 100 = 83$ %.

1.2.2 Catalyst

The task of the catalyst is to split the incoming reactant gases into intermediate products and boost the reaction rate in the FC. One one the main advantages of the AEMFC is the prospect of using non-noble catalysts for bot the anode and cathode reactions [6]. However today the the vast majority of catalysts used in FCs are made from Pt [7].

AEMFC catalysts are available for \$10 per sq ft [2, ch. 5.4.4] at the current stage of FC use in society this is a bearable cost for the industry. However as the use of

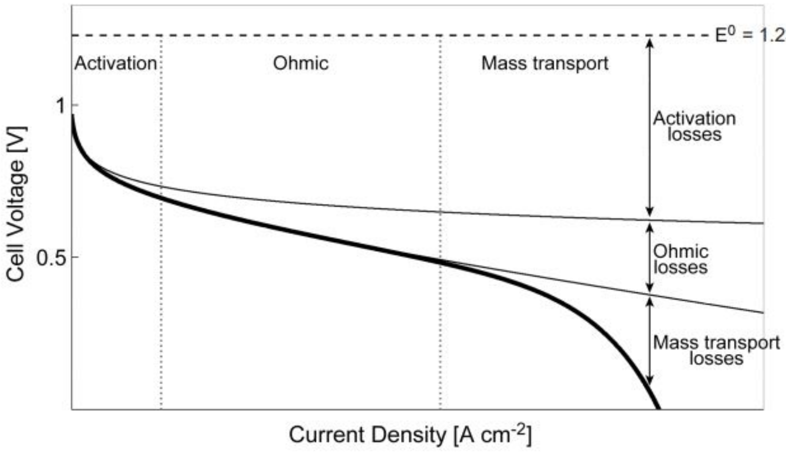

Figure 1.2: A figure showing a typical polarisation curve of a FC [2]

FCs increases and production cost decrease the cost of the catalyst will approach a large portion of the entire system cost and therefore hinder further FC expansion of a renewable hydrogen economy. To combat this, the there is a need to develop catalysts with a mass activity (activity per mass of Pt) as high as possible, along with alternatives using to Pt as the catalyst[7].
Alternatively in the quest to minimise the amount of Pt needed for catalysts the way forward may be to develop support with a structure as similar as possible for the Pt and thereby be able to coat only a few atomic layers of Pt on top while still retaining the qualities of bulk Pt. Tungsten carbide (WC) is known to have a structure similar to Pt [8],[9] this potentially means a WC and Pt would work well with a good lattice match. WC also has a lot of features promising for use in the FC environment such as good resistance to oxidation and heat, little thermal expansion and good electrical conductivity. All this combined makes WC a good candidate for such support.

1.2.3 I-V curves and overpotential

From the operating potential we can also extract the FC overpotential as $\eta_{OP} = U_{cell} - 1.23$ V (* not the same as efficiency in eq. (1.6)). As the overpotential are direct losses for the FC system the overpotential are essential to reduce to increase the efficiency of the system. A normal operating voltage curve of a FC is displayed in in fig. 1.2.
As can be seen in fig. 1.2, there are three mayor types of losses in a FC:

- Activation losses
- Ohmic losses
- Mass transport losses

The majority of the overpotential is due to activation losses. These are due to slow reaction kinetics at the catalyst surfaces. Through reducing these losses the efficiency of the FC can be directly reduced. Ohmic losses are due to electric resistances in the FC and are essentially proportional to current in the FC. Mass transport losses stem from reactants not being transported fast enough to the catalyst causing a potential drop due to low concentrations of reactants.

1.3 Aim

This work aims to contribute to catalyst development through studying the effect of using WC as support for the cathode catalysts in an AEMFC. Parameters for annealing of the application of WC thin films will be studied as well as hydrogen reducing. Following this the performance of WC supported catalysts will be tested for the ORR reaction. The tested catalyst layer will be Pt, Pd, Cu and Ag.

2

Theory

The samples were fabricated using DC magnetron sputtering and physical vapour deposition. In order to test the developed catalyst surfaces they were studied using a rotating disc electrode (RDE) controlled by a potentiostat. This model system allows to study the reaction kinetics of the electrode surface. Along with this the electrode surface were studied using scanning electron microscopy (SEM) giving an image of what the surface morphology looks like.

2.1 Measurements of Potentials

The main goal of a good catalyst is to give a high activity with an overpotential as low as possible in order to have low activation losses fig. 1.2. To study how the tested catalysts perform their performance were studied in an model system. This way the half cell reaction namely the ORR can be studied separately. The system employed was a three electrode setup submerged in an alkaline electrolyte. The three electrode setup is illustrated in fig. 2.1.

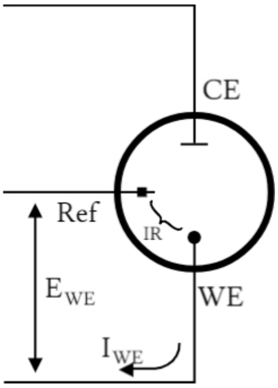

Figure 2.1: Schematic of a three electrode system.

Through this setup the current at the catalyst surface can be recorded while the potential is controlled. The recorded current I_{WE} and potentials then gives insight of the quantity of reacted species at the catalyst surface. For a constant potential the moles of reacted material n_j is given by Faraday's law as

$$n_j = \frac{Q_{WE}}{Z_j F} \tag{2.1}$$

Z_j is the charge on one molecule, F is Faradays constant (96487 C), and $Q_{WE} = \int I_{WE} dt$ is the total charge [10, eq. 1.11]. From this we can also get the reaction rate of the reaction as

$$k_j = \frac{dn_j}{dt} = \frac{i}{Z_j F} \tag{2.2}$$

In the equation above eq. (2.2) the current is essentially proportional to the surface area. Therefore the current is often expressed as the current density as $j = \frac{i}{Area}$. A point to consider however is the meaning of surface area, as at the nano/micro scale the surface may be very convoluted rather than flat. To measure the number of active sites on the catalyst the electrochemical surface area (ECSA) is commonly used. This differs from geometrical surface area through integrating all of the area of the microscopical peaks and troughs. This is an important measure since it offers a way to characterise the current density of catalyst with respect to their morphology. This is to counteract the effect that catalysts with high surface area could have many more catalytic sites than a catalyst with a flat surface. This will be further elaborated in section 2.1.5.

2.1.1 Electrochemical equilibrium and Nernst equation

Consider the ORR reaction stated in 1.2. The chemical potential of the species in the reaction is the change in Gibbs free energy ∂G divided by the change in molar quantity ∂n_j which can be expressed as

$$\mu_j = \left(\frac{\partial G}{\partial n_j}\right)_T \tag{2.3}$$

at contant temperature and pressure [11, eq 1.4]. Where j is any of the species $\mathrm{O_2, e^-, H_2O, OH^-}$. Therefore at chemical equilibrium the total chemical potential of the reaction will be

$$2\mu_{O_2} + 4\mu_e^- + 2\mu_{H_2O} = 4\mu_{OH^-} \tag{2.4}$$

Under conditions with the species in the reaction in aqueous solution the chemical potential can also be written

$$\mu_j = \mu_j^0 + RT\ln\left(\frac{\gamma_j c_j}{c_0}\right) \tag{2.5}$$

where R = 8.314 $JK^{-1}mol^{-1}$ is the universal gas constant , T is the absolute temperature in Kelvin, γ_j is a non ideality factor, c_j is the concentration of element j and c_0 is the standard concentration of one molar. [11, eq. 1.12]. Putting eq. (2.5) and eq. (2.4) together we acquire the standard Gibbs energy change in the reaction as

$$\Delta G = -RT\ln K_{ORR} \tag{2.6}$$

where the equilibrium constant K_{ORR} is given by

$$K_{ORR} = \frac{\gamma_{O_2}^2 c_{O2}^2}{\gamma_{OH^-}^4 c_{OH-}^4} \tag{2.7}$$

To account for the influence of the electron needed in the reaction, an alteration is needed in the expression for the chemical potential.

$$\bar{\mu_j} = \mu_j + Z_j F\phi = \mu_j^0 + RT\ln\left(\frac{\gamma_j c_j}{c_0}\right) + Z_j F \tag{2.8}$$

[11, eq. 1.30] ϕ is the electric potential at the molecule. This causes some delicate need for consideration regarding the electrical potential ϕ. All molecules taking part in the reaction are in the potential of the electrolyte solution ϕ_s, while the electrons are at the same potential as the metal ϕ_m. Putting eq. (2.8) and eq. (2.5) in eq. (2.4) and rearranging the terms we get the Nernst equation

$$\phi_m - \phi_s = \frac{\Delta\mu^0}{F} + \frac{RT}{F}\ln K_{ORR} \tag{2.9}$$

with the constant $\Delta\mu^0 = 2\mu^0_{O_2} + 4\mu^0_{e^-} + 2\mu^0_{H_2O} - 4\mu^0_{OH^-}$. This, however, only gives us the equilibrium of the studied reaction, as the ORR studied reaction in no way can be said to have reached equilibrium during the experimental process to get insight in the dynamic process during running further consideration is needed.

2.1.2 Electrode potentials and reference electrodes

Before discussing the electrode kinetics a word on electrode potentials is in order. As can be seen in eq. (2.9) the potential is only measured as the difference between the electrolyte and the electron supplying surface, i.e. electrode. This means that in order to know the potential difference between the surface ϕ_m and the solution ϕ_s another electrode is needed. This is the reason for the use of a reference electrode as seen in fig. 2.1. The reference electrode is an redox-pair with a known potential that is submerged in the solution. The redox pair is enclosed but is in contact through a small glass frit, in order to avoid contamination of the electrolyte solution. Through knowing the potential difference between the electrolyte and the solution one can calculate the relative potential at the working electrode surface (WE in fig. 2.1. With two different electrode surfaces in the electrolyte the difference between them is now the measured quantity as

$$E_{WE} = \phi_{m,WE} - \phi_s - \phi_{m,Ref} - \phi_s + E_{IR} \tag{2.10}$$

where the extra term $E_{IR} = Ru * I_{WE}$ is the due to the internal resistance R_u of the cell between the reference and the working electrode (see fig. 2.1). This is simply an ohmic resistance in series with the measurement and its effect can therefore be subtracted if the resistance is known. The internal resistance of a cell is readily measured using impedance spectroscopy as described in [12]. When no current is run the cell the E_{WE} becomes the electromotive force of the cell E^0.

This the measured potential will always be *versus* a reference, most commonly the reversible hydrogen electrode (RHE). Because of practical considerations in this case the RHE was not a feasible electrode. Therefore the the data must be translated to be reported versus the RHE through the use of tabulated reference electrode values.

Furthermore to ensure that the reference electrode is at a stable equilibrium a large net current cannot be run through it. Therefore a counter electrode is necessary to run the current without disturbing the potential measurement. [11, sec.2.2]. A rod of porous graphite provides the large surface area to ensure the reaction can run.

2.1.3 Electrochemical double layer

When a reaction such as 1.2 takes place as stated in Nernst equation, a potential difference will build up across the surface. As the electrode is a conductor the mobility of the ions will force any free charges inside the electrode to be on the surface its surface. This will in turn attract the oppositely charged ions in the electrolyte [10, sec 3.4]. This is the origin of the Helmholtz-layer (see fig. 2.2). Depending on the strength of the potential difference the layer can be more or less fully covering.

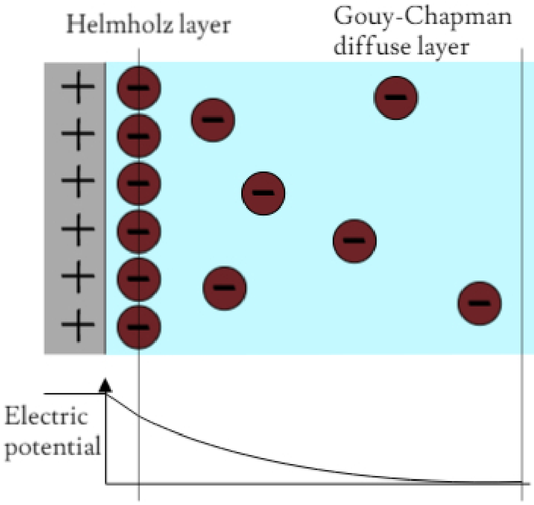

Figure 2.2: Illustration of the electrochemical double layers, along with an graph of how the potential decreases into the electrolyte.

Outside of this inner layer a more mixed layer will form, this is termed the Gouy-Chapman diffuse layer and will consist of a gradient of charged species. Making it able to vary how much it extends from the surface. The thickness of the double layer for a 0.1 M electrolyte is on the order of 1 nm [10, sec. 3.4.1], though this is strongly affected by many parameters this will be a useful fact later.

2.1.4 Capacitive ECSA measurements

If the potential across the surface E is altered the magnitude of the double layer will grow or shrink to match the charge build up on the electrode. The formation of this layer works much like the charge build up inside a capacitor. Subsequently any potential change of the electrode will be associated with a corresponding current. The current in the working electrode will therefore constitute the sum of two currents $i_{WE} = i_{cap} + i$. The capacitive current can be expressed as [10, eq. 3.143]

$$i_{cap} = C_{dl} * \frac{dE}{dt} \tag{2.11}$$

where the C_{dl} is the surface capacitance and $\frac{dE}{dt}$ is the scan rate at which the voltage is being changed. Given that the capacitive current i_{cap} can be isolated this offers a way of ECSA as is described in [13]. If the acquired value for C_{dl} is compared

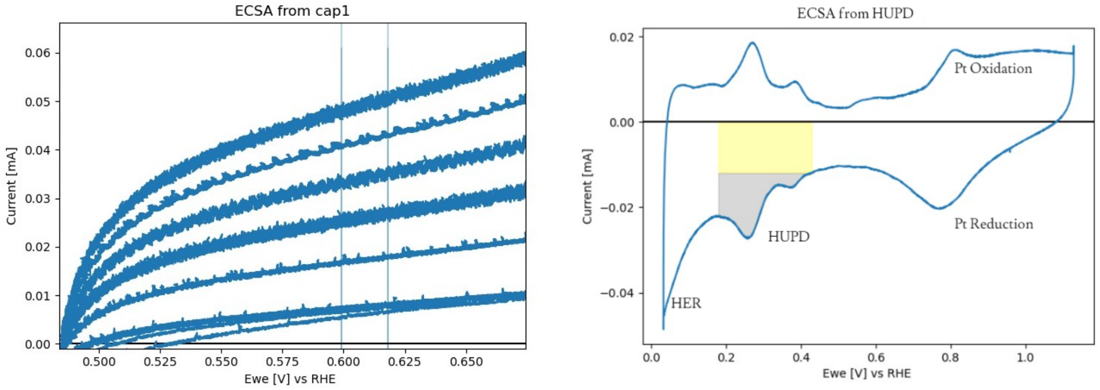

(a) **(b)**

Figure 2.3: a) Figure showing a capacitive ECSA measurement. Each set of lines are at different scan-rates. The capacitance is studied in the region between the two vertical lines. b) CV of Pt for H_{UPD} measurement. The peaks are marked with their corresponding reaction. The region in gray corresponds to the charge associated with H_{UPD}. Both plots are chosen to be representative of the phenomenon.

with the known specific capacitance from literature C_S of a surface with a known size and identical composition one can acquire a value for the ECSA of the current surface.

$$ECSA_{cap} = \frac{C_{dl}}{C_S} \tag{2.12}$$

Practically this is done through varying scan rate in a potential range where there is as little electrochemical reactions taking place as possible. An example of such a measurement is fig. 2.3a.

As is stated in [14], however, this method depends strongly on the chemical state of the surface. Therefore this method will be used mainly to determine the change in the surface before and after the ORR reaction.

2.1.5 ECSA from H_{UPD} charge or surface reduction charge

Another way of measuring the ECSA is through H_{UPD} as described in [14, sec. 2.4]. Here the area of hydrogen is measured using the adsorption charge of hydrogen on Pt. Comparing this with a known value for surface charge of an essentially atomically flat surface the area can be deduced. The H_{UPD} surface charge of Pt is 210 µC/cm^{-2}[14]. In the case of pure Pt surfaces this available as a current peak found before hydrogen evolution reaction (HER) in the CV (see fig. 2.3b).

For reduction peak measurements the process is essentially the same just that the measured charges are due to surface oxidation instead of H_{UPD}. The surface charge used varies from material to material however which can cause complications. ECSA measurements through reduction peaks is however less accurate [15] than $ECSA_{HUPD}$.

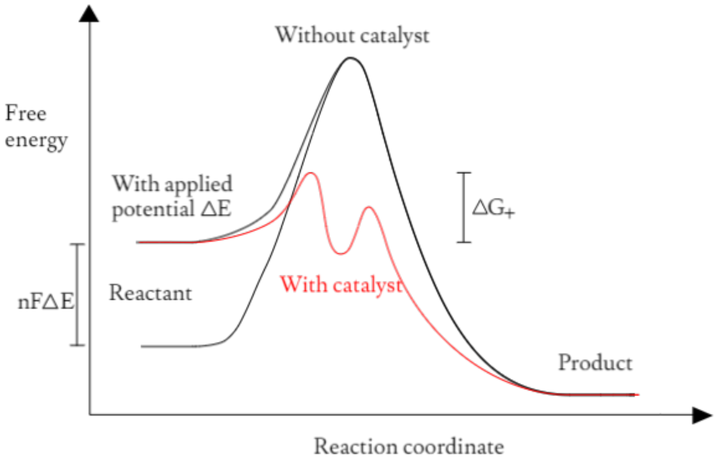

Figure 2.4: Energy levels of reactants in three different cases, With no applied potential and no catalyst, with applied potential and no catalyst and with applied potential and a catalyst (red). In the case with a catalyst the intermittent steps are in a lower energy state due to their interaction with the surface.

2.2 Kinetics and overpotential

So far the discussion has only entailed electrochemical equilibrium, this will now be broadened to a discussion regarding parameters that control the reaction rates and the effect of a catalyst. For the case of simplicity the focus will be on the cathodic direction of reaction but the reverse reaction is follows the same logic.

2.2.1 Activation energy and the Arrhenius equation

Any reaction involving the transition of species A from an oxidised state to a reduced state can be be written as eq. (2.13). k^- is the cathodic reaction rate and k^+ is the anodic reaction rate.

$$\mathrm{A_{ox}} + \mathrm{n}^- \underset{k^+}{\overset{k^-}{\rightleftharpoons}} \mathrm{A_{red}} \tag{2.13}$$

To explain the underlying cause of the reaction rates activated complex theory can be used. An illustration of this is usually done using reaction profiles where the Gibbs energy of the system is plotted against a reaction fictous coordinate as seen in fig. 2.4. This illustrates the fact that the reactants need to pass through a state of higher energy in order to reach the end product. The figure shows a reaction with one intermediate product, in reality however there may be many intermediate products and the actual energy levels may be much more complicated.
The energy needed to pass through the activated complex for the case with an applied potential and a catalyst is noted in fig. 2.4 as ΔG_+. If the potential at the electrode is more negative, the free energy of the electrons at the surface will then decrease (as is shown in fig. 2.4). The change can be expressed as

$$\Delta G = \Delta G_0 + \beta n F \Delta E \tag{2.14}$$

[10, eq. 4.9] where β is the so called asymmetry parameter and ΔE is an applied electric potential and G_0 is energy barrier with out applied potential. To express the cathodic reaction rate shown in eq. (2.13) the Arrhenius equation gives the reaction rate [10, eq4.49]

$$k^- = c_{ox}k^0 e^{\frac{-\Delta G}{RT}} = c_{ox}k^0 e^{\frac{-\Delta G_0}{RT}+\frac{\beta nF\Delta E}{RT}} \tag{2.15}$$

$c_{red/ox}$ is the concentration of reactants, k^0 is a pre-exponential factor. With a catalyst present the intermediate products interact with the surface which lowers the energy of the system. This causes the energy barrier the to be lowered which can increase the reaction rate dramatically according to eq. (2.15).

The reaction rate is heavily dependant on the potential barrier ΔG however the as ΔG_0 does not depend on the applied potential this can be incorporated into the rate constant k^0. Expressing the reaction rate in terms of the overpotential $\eta = E - E^0$ gives

$$k^- = k^{00} e^{-\frac{\beta nF}{RT}(E^0-\eta)} \tag{2.16}$$

Using $i^- = nFk^-$ 2.2 and epressing as current density this can be further simplified by breaking out the exchange current density j_0 [10, eq. 4.22a]

$$j^-(\eta) = -j_0 e^{-\frac{\beta nF\eta}{RT}} \tag{2.17}$$

analogously the anodic current density can be expressed as [10, eq. 4.22b]

$$j^+(\eta) = -j_0 e^{-\frac{(1-\beta)nF\eta}{RT}} \tag{2.18}$$

2.2.2 Exchange current density and Tafel equation

As shown in reaction eq. (2.13) both the oxidation reaction and the reduction reaction take place at the same time. As they are opposites of each other this will result in only the net rate being visible at a macro scale. We can get the total current as the sum of the oxidation current and the reduction current eq. (2.17)

$$j = j^- + j^+ = j_0 \left(e^{\frac{(1-\beta)nF\eta}{RT}} - e^{\frac{-\beta nF\eta}{RT}} \right) \tag{2.19}$$

giving the *Butler-Volmer equation.* The value j_0 is one of central essence as this determines the magnitude of the reaction rates caused by a unit change in η. It is therefore to increase j_0 that will be the the mayor focus of a catalyst.

For values of large $|\eta| > RT/nF = 25.7$ mV the only one of the reactions in eq. (2.19) needs to be considered while the other goes to zero. Taking the logarithm of eq. (2.17) we can obtain the *Tafel equation* [10, eq.4.26]

$$log_{10}|j| = log_{10}j_0 + \frac{\beta nF}{2.303RT}|\eta| \tag{2.20}$$

Which is gives a neat relationship between applied overpotential η and the current density.

2.2.3 Current limitation due to reactant concentration

For eq. (2.20) to be valid, η needs to be small enough for the reaction to only be controlled by the electron transfer rate. For large $|\eta|$ the current density can be large enough large enough cause lower concentration at the electrode surface. Since at equilibrium potential E^0 the net current is zero, the *Butler-Volmer eq.* eq. (2.19) can be used to find an expression for the concentration dependence of the the exchange current density as [10, eq. 4.38]

$$j_0 = Fk_0(c_{ox}^{(1-\beta)} c_{red}^{\beta}) \tag{2.21}$$

From this it is evident that a drop in concentration at the electrode surface would have a strong effect on the current density of the reaction. There is therefore two different limiting mechanisms on the reaction rate, the *charge transfer rate* at which the charge is transfered across the interface at the catalyst surface and the *mass transport rate* which is the rate at which reactants are transported to the electrode. For a current limiting by diffusion and by kinnetics at the electrode the overall current is given by the Koutecky-Levich equation

$$\frac{1}{i} = \frac{1}{i_k} + \frac{1}{i_d} = \frac{1}{j_k} + \frac{1}{B\omega^{1/2}} \tag{2.22}$$

$$B = 0.2D^{2/3}\nu^{-1/6}n_{KL}Fc_{\infty}$$

With c_{∞} being the bulk concentration of the reacting species, D the diffusion coefficient, ν the kinematic viscosity of the electrolyte and n_{KL} the electron transfer coefficient (number of electrons transfered per reaction). [5]. Through plotting j^{-1} vs $\omega^{-}1/2$ eq. (2.22) gives an easy way of obtaining the kinetic current j_k as the intercept of the acquired curve, and the number of electrons participating in the reaction n_{KL} (explained in section 2.3). This is only valid however, when the reaction is one-step,one-way, and first-order. The expression for n_{KL} is

$$n_{KL} = \frac{\partial \omega^{1/2}}{\partial j} * \frac{1}{0.2D^{2/3}\nu^{-1/6}Fc_{\infty}} \tag{2.23}$$

From eq. (2.22) it is also evident that at a constant rotation rate ω as the potential is changed, at high overpotential the current will be limited by the mass flux, this will lead to the ORR curves having a sigmoid shape.

2.2.4 Mass transport

The processes of electron transfer take place through quantum mechanical tunneling [11, sec.2.1], this leads to the reaction having a very short length in which the reaction can happen. This leads to a situation where products must be transported away from the surface and reactants must be transported in, illustrated in fig. 2.5. Three different mechanism are available to supply the surface with reactants.

- Diffusion, due to a concentration gradient
- Convection, due to flow
- Migration of charged species driven by a potential

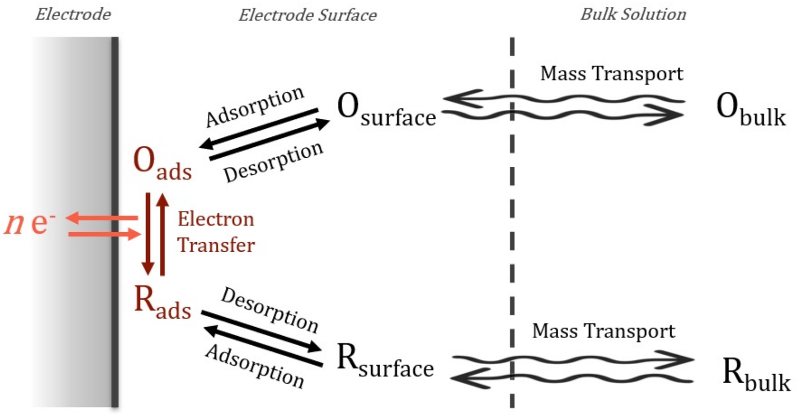

Figure 2.5: Illustration of the mass transport at the surface.

The sum of all this gives a very complex behaviour dependant on a large set of parameters as well as effects from turbulence in the cell. To mitigate this a rotating disk electrode (RDE) is commonly used. The RDE is rotated at a controlled speed ideally giving a steady laminar flow over the surface. Using this one can control the mass transport limitation of the current. Thereby using eq. (2.22) one can extract values for the the charge transfer rate of the reaction [16].

2.2.5 Electrocatalysts

The main focus of this work is to test catalysts for the ORR reaction. The goal of this heterogeneous catalyst is to increase the exchange current density of the reaction taking place at the surface, commonly referenced as the intrinsic activity of the catalyst. A basic explanation of how the catalyst is able to increase the reaction rate can be developed from fig. 2.4. There we see the transformation of $A_{ox} + n^- \rightleftharpoons A_{red}$ via an intermediate step. This intermediate step bound to the surface can consist of many small sub-steps or even entail multiple different pathway from A_{ox} to A_{red}. The role of the catalyst in this situation however is to lower the energy for the intermediate products. This can be done through increasing or lowering the bonding energy of the reaction intermediate. Through doing this the activation energy needed is decreased and subsequently the eq. (2.15) predicts a faster reaction rate.

This is known as the *Sabatiers principle* which can be summarised as the binding energy of the intermediates should be *just right* for the current density to be at its maximum. Sabatiers principle gives rise to Volcano plots an example of which is found in fig. 2.6. In such a plot the binding energy of certain species of plotted against the activity of a catalyst. Different elements are represented as points in the volcano plot. Worth noting is also that the activity axis is commonly the logarithm of activity, which indicates that even small increases in the plot may have a very large effect for the reaction rate.

As mentioned in section 1.2.2 the most common catalyst material in FCs is Platinum and correspondingly Pt is found almost at the top in fig. 2.6. The fact that Pt is

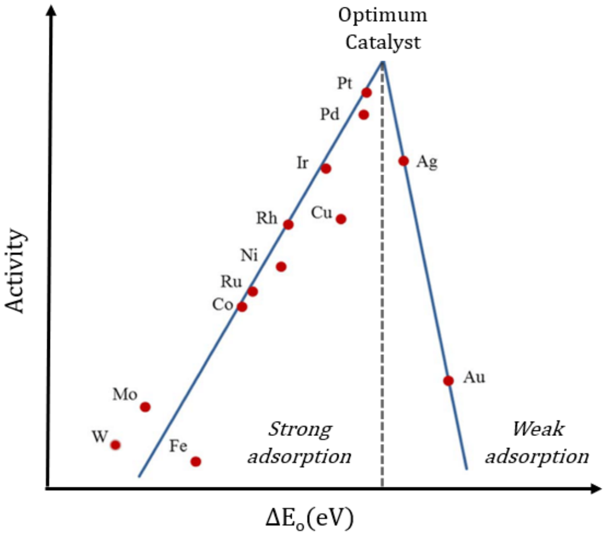

Figure 2.6: Volcano plot for the activity of the ORR reaction on different elements versus the adsorption energy, used with permission from [17]

one of the rarest elements on earth however [18] bring some obvious downsides. The volcano plot therefore offers a good place to start when looking for alternatives.

2.3 Electron transfer coefficient with RRDE - n_{RRDE}

As mentioned in section 1.2 the ORR reaction has two main reaction pathways, the 2e or the 4e pathway.

$$\begin{aligned} &O_2 + 2H_2O + 4e^- \rightarrow 4OH^- && 4e \\ &O_2 + H_2O + 2e^- \rightarrow HO_2^- + OH^- && 2e\ (1) \\ &HO_2^- + H_2O + 2e^- \rightarrow 3OH^- && 2e\ (2) \end{aligned}$$

As the 4e pathway is preferred [5] finding which pathway is dominating is important. This is commonly measured as the average number of electrons participating in the reaction called the electron transfer coefficient n_{RRDE}. Two methods are commonly employed to do this. The first method is to have a Pt ring at a fixed distance outside the catalyst disk, referred to a rotating ring disk electrode (RRDE) see fig. 2.7. The ring is held at a constant potential (commonly 1.2 V vs RHE) whereby it reduces H_2O_2 that passes by. With this the n_{RRDE} can be computed through measuring the current in the ring as

$$n_{RRDE} = 4 \times \frac{i_{we}}{i_{we} + i_{ring}/N_c} \tag{2.24}$$

where N_c is the H_2O_2 collection efficiency. This offers an efficient way of calculating the electron transfer number for every potential of the ORR reaction. One issue in

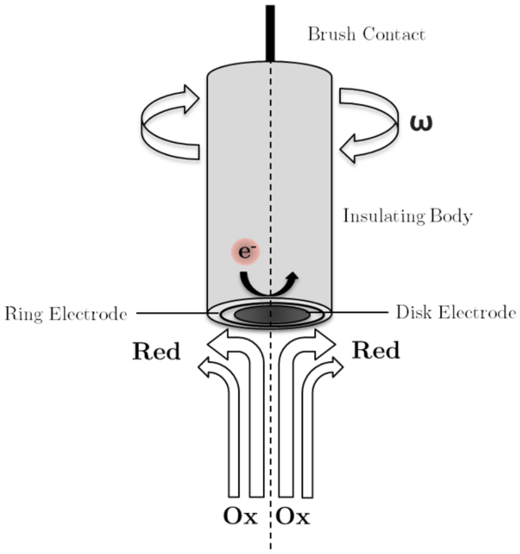

Figure 2.7: Illustration of an RRDE. Used with permission from [17]

KOH electrolyte raised by Zhou et al. however is that the the use of Pt as the ring is sub-optimal and ideally Au rings should be employed [5]. In this study however no Au ring was available and a Pt ring was used. Furthermore for Zhou et al also states that for rough electrodes the collection efficiency N_c decreases rapidly with increasing ω.

2.4 Fabrication methods

In order to study WC thin films as a support for different active layers, thin films of WC can be laid on a substrate using thin film techniques such as DC magnetron sputtering and physical vapour deposition. Using theses techniques thin films can be made in to an almost any thickness. This gives a good opportunity to precisely control the amount of deposited material and to isolate the effects of very thin films of the deposited elements. The thickness of the film can be controlled using the deposition time.

All techniques involve a target and a substrate, the target is the material which is kicked of and deposited on the substrate. Next follows a short description in the essentials of how the techniques work.

2.4.1 Sputtering

During sputtering a large potential (around 1 kV) is held between the sputter target and the substrate. A sputter gas (typically argon) is then introduced, which is ionized using a magnetron close to the sputter target. The ionised argon atoms are accelerated towards the target knocking out clusters of atoms at impact. The clusters subsequently proceed to impinge on the substrate where they form a thin film. A setup sketch can be seen fig. 2.8 [19]

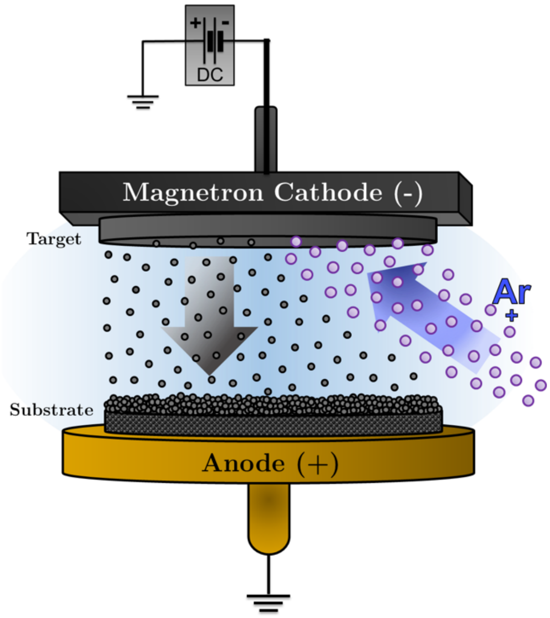

Figure 2.8: A schematic illustration of a sputter. Used with permission from [17]

Through controlling the base pressure of argon the directionality of the sputtering can be controlled. A higher base pressure gives more molecular collisions for the molecules between the target and the substrate thus reducing the directionality of the deposition. A lower directionality means that the sublimation process produces a better film quality since it is able to reach in to the small pores on the substrate. An issue in the case of the multi-elemental sputtering is that the different elements require different energy to be kicked out. In the case of WC it is not known to what extent this affects the substrate film composition.

2.4.2 Electron-beam physical vapour deposition

Electron beam physical vapour deposition (EB-PVD) is a process where a thin film is made from gases precipitating on to the surface. A sketch of an EB-PVD setup can be seen in fig. 2.9, the whole setup is held vacuum.
An electron beam of a few μA with an acceleration voltage in the range of 10 kV is fired on to a target, this creates a lot of heat which causes the target to sublimate. The gaseous atoms fly from the target on to the substrate where they de-sublime and form a film.

2.4.3 Annealing and reduction in H_2

After the W_xC has been sputtered it is likely not composed of crystals of appropriate size and composure as has been reported in [13]. To further treat it it is therefore annealed. This entails heating to high temperatures for a certain amount of time. During this time the atoms rearrange and the crystals coalesce. The process reduces internal stress and forms stochiometric crystals of W_xC. In the phase diagram om

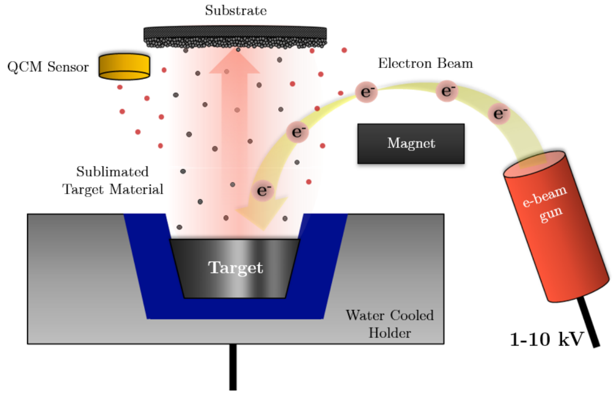

Figure 2.9: Principle of electron beam physical vapour deposition. Used with permission from [17].

W_xC there are two possible crystal structures WC and W_2C (see fig. 2.10). As the ratio of W vs C is not known, the thin film likely contains both WC and W_2C to a varying degree and the supporting film is labeled W_xC.

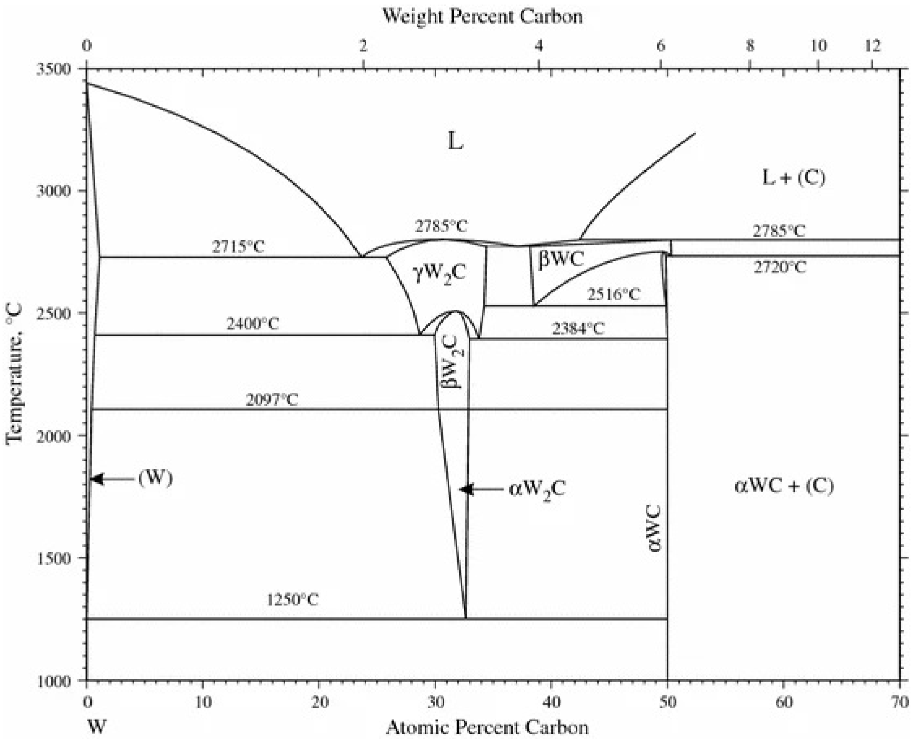

Figure 2.10: Phase diagram of W_xC, used with permission [20].

After annealing process the surface likely contains oxides and regions of graphitic carbon. To remove these layers the surface is heated in another furnace in a hydrogen rich environment. This removes oxide and graphitic parts leaving only the W_xC.

3

Methods

To test the W_xC thin films as substrate material, different catalysts where coated onto glassy carbon electrodes. These were then measured in a RDE, and subsequently studied using SEM and XRD. This was an iterative process where initially samples were tested with the aim of finding the right treatment process. This aimed to identify the most suitable annealing temperature and the conditions for hydrogen treatment of the samples. Following this, a study of different catalyst materials and subsequently a longer test to ensure some stability of the samples was carried out. The test were tested against standard benchmark catalyst of Pt, Pd, Cu and Ag, these samples were also fabricated.

3.1 Sample Fabrication

The samples were fabricated using a range of different processes. A complete table of all samples presented in this thesis is found in table 3.1. The samples were all evaporated onto glassy carbon cylinders. The cylinders are 5 mm in diameter and have a height of 4 mm. A sketch of the GC is shown in fig. 3.1.

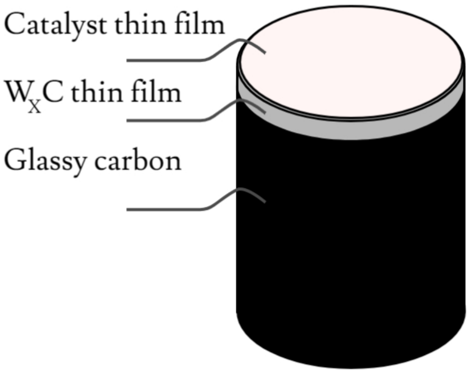

Figure 3.1: Illustration of glassy carbon sample.

Comment	Nr	Sample name	Plasma cleaned	Annealing temperature	H_2-treatment	W_xC layer	EB-PVD layer (catalyst layer)
W_xC annealing	1	W_xC - 700 C		700 C	-	40 nm	-
	2	W_xC - 1100 C		1100 C	-	40 nm	-
	3	W_xC - 1400 C		1400 C	-	40 nm	-
W_xC H_2 reduction	4	W_xC - H_2 - 700 C		700 C	H_2 - 700 C	40 nm	-
	5	W_xC - H_2 - 1100 C		1100 C	H_2 - 1100 C	40 nm	-
	6	W_xC - H_2 - 1400 C		1400 C	H_2 - 700 C	40 nm	-
W_xC annealing + Pt	7	W_xC - 700 C - Pt		700 C	H_2 - 700 C	40 nm	3nm Pt
	8	W_xC - 1100 C - Pt		1100 C	H_2 - 1100 C	40 nm	3nm Pt
	9	W_xC - 1400 C - Pt		1400 C	H_2 - 700 C	40 nm	3nm Pt
Catalyst	10	W_xC Pt		1400 C	H_2 - 700 C	40 nm	3nm Pt
	11	W_xC Pd		1400 C	H_2 - 700 C	40 nm	3nm Pd
	12	W_xC Cu		1400 C	H_2 - 700 C	40 nm	3nm Cu
	13	W_xC Ag		1400 C	H_2 - 700 C	40 nm	3nm Ag
Reference catalysts	14	GC Pt	✓	-	-	-	40 nm Pt
	15	GC Pd	✓	-	-	-	40 nm Pd
	16	GC Cu	✓	-	-	-	40 nm Cu
	17	GC Ag	✓	-	-	-	40 nm Ag
References 3nm catalysts	18	GC 3nm Pt	✓	-	-	-	3nm Pt
	19	GC 3nm Pd	✓	-	-	-	3nm Pd
	20	GC 3nm Cu	✓	-	-	-	3nm Cu
	32	GC 3nm Ag	✓	-	-	-	3nm Ag

Table 3.1: All presented samples in this thesis. Refer to different method sections for more detailed descriptions about the fabrication methods. Samples marked '-' were not treated with the technique. The first column gives a indication of what was studied in the sample series.

3.1.1 Pre-fabrication cleaning protocol

Initially, before any layer was added to the GC, they were cleaned. This was done in a four step process as follows:

1. Ultrasonicate GC:
    (a) Acetone in ultrasonicator - min
    (b) Isopropanol in ultrasonicator - 10 min
    (c) H_2O in ultrasonicator - 10 min
2. (Plasma clean in Dry etch RIE - Plasma-Therm - Oxygen, 100 W for 1 min)

The last step was only done on the reference samples.

3.1.2 WC sputtering

The process of sputtering W_xC was done in a home built DC sputter at the division of Chemical Physics at Chalmers. The process parameters were as written in table 3.2.

3.1.3 Annealing and H_2 treatment

After sputtering the samples were annealed using a *Thermolyne Open Tube Furnace*. This entailed heating the samples starting at room temperature increasing the temperature 5 C/min until the furnace had reached the the set annealing temperature

Base pressure	$1.9 * 10^{-8}$ mBar
Sputtering gas	Argon
Argon flow rate	300 sccm
Voltage type	DC
Voltage	300 V
Sputter power	20 W
Target	WC
Goal thickness	40 nm
Sputtering time	10 min
Temperature	Room temperature

Table 3.2: WC sputtering parameters used for thin film deposition of W_xC on GC in Sputty.

as stated in 'Annealing temperature' in table 3.1. The furnace was then kept at that temperature for 30 min, followed by cooling of until room temperature.
After the annealing the samples were treated in a *Centrotherm High Temperature Furnace* hydrogen furnace. The samples were there treated at the temperature stated in the '$H_2 - treament$' column in table 3.1.

3.1.4 Active thin film EB-PVD

The application of the final layer was done using electron beam physical vapour deposition (EB PVD) in a **LESKER PVD225** with the process parameters showed in table 3.3. This process was automated and run entirely by the LESKER software

Base pressure	$< 6.66 * 10^{-7}$ mBar
deposition rate	1 Å/s
EB voltage	10 kV
EB Current	100 mW

Table 3.3: Values of parameters used for EB-PVD.

with the only being was the target thickness of the sputtered layer.

3.2 Electrochemical measurement procedure

After sample fabrication was done, the samples were studied in an RDE setup using a BioLogic SP-300 potentiostat. The laboration setup was done according to the protocol laid out in [21]. Although each new sample gave slightly different results, for the sake of systematicity the laboration followed largely the same steps. The laboratory steps were as follows:

1. Approximately 150 ml of 0.1 M KOH was added to a Teflon cell cleaned in milliQ H_2O.
2. The cell was connected using a $Hg/HgSO_4$ reference electrode and a graphite counter electrode.

3. A flow of argon of ~ 0.2 Nl/min was babbled in the cell. During this time the disk was rotated at 200 rpm.
4. The internal resistance R_u of the cell was measured using EIS as described in [22] and [23]. Following this E_{IR} was compensated for.
5. A CV with scan rate 50 mV/s and an average over 10 points was performed. The operational range can be seen in the results [24].
6. Several CVs were recorded at different scan rates (50, 100, 150, 200, 250, 300 mV/s), at the potential range of the flattest region of the full CV to record the capacitive current of the cell.
7. The Argon babbling was changed to Oxygen and the cell was left as in step 3 for 15 minutes with rotation.
8. The ORR activity was measured using a CV with increasing rotation on the electrode. Three cycles were made at each rotation rate. The rotation rates were 0, 400, 900, 1600, 2500 rpm. scan rate = 50 mV/s, CV vertexes were $E_1 = 0$ V and $E_2 = 1.0\ V_{RHE}$
9. Finally, steps 3 - 6 were repeated to measure the change of R_u and ECSAs during ORR measurement.

During the electrochemical measurement the system was on-line IR-compensated to 85 % as state in step 3. This improves the potential accuracy, as the setpoint values in the ideal case only dependant of 15 % of the internal resistance. As stated by BioLogic, it is not advisable to compensate 100 % during measurements as this can lead to system instability [25, sec. 2.6.2].

3.3 SEM imaging method

SEM images of the samples were taken before and after RDE measurements. This was done both in a *SEM - Zeiss Supra 55* with an in lens detector at 5 kV acceleration voltage and the samples were kept a working distance of ~ 5 mm. First secondary electrons were used to focus the SEM and after that pictures were taken using backscattered electrons.

3.4 Data analysis method

From the data acquired during the ORR step of the measurement the onset potential E_{onset}, limiting current i_{lim}, half max current $E_{1/2}$, kinetic current j_k and electron transfer coefficient from RRDE n_{RRDE} and Koutecky-Levic n_{KL} are extracted. From the CVs in step 3 - 6 and 9 in section 3.2 the ECSA and uncompensated resistance R_u was acquired.

In order to extract the performance characteristics from the ORR the a python script was used. In short the method can be described as the following. Three lines were adapted as showed in fig. 3.2 numbered line 1, 2 and 3. The intersections of these intersection of line 1 & 2 was used as the maximum current. The onset potential was set to when the cathodic current had reached 1 % of the i_{lim} and the half max current $E_{1/2}$ is the potential where current is 50 % of the limiting current. All of the above follows the method described by Get et al. [3].

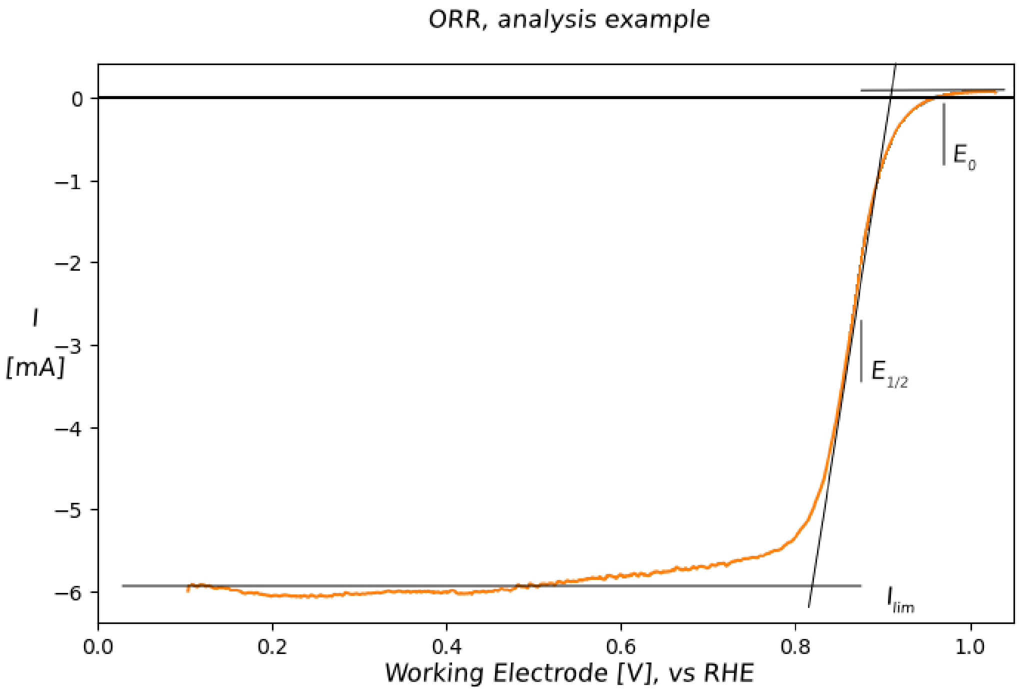

Figure 3.2: Illustration of how data was analysed as described in section 3.4, this is the cathodic sweep from an arbitrary data sample rotating at 1600 rpm and with a scan rate of 50 mV/s. E_o is the onset potential, $E_{1/2}$ is the half max potential, I_{lim} is the limiting current density.

4

Results and discussion

All numerical results are summarized in table 4.1 and will be discussed in the order of study. Initially the study aimed at finding the right annealing temperature and H_2 treatment parameters. Following this is a discussion regarding measuring the ECSA for the different samples and finally testing different catalytic materials evaporated onto the thin W_xC thin films substrate.

4.1 Annealing and $\mathbf{H_2}$ treatment of Sputtered $\mathbf{W_xC}$ thin films

Before catalyst layers were able to be tested with the W_xC it was necessary to test out a fabricating procedure for W_xC thin films. This was done by fabricating many samples and anealing them at different temperatures as well as testing with or without hydrogen reducing. ORR polarisation curves, $ECSA_{HUPD/Red.}$, $HUPD_{cap}$ was recorded and SEM images were taken for all samples. This was done to find the most suitable fabrication process.

Nr	Sample name	Onset potential E_O [V vs RHE]	Half max $E_{1/2}$ [V vs RHE]	$ECSA_{HUPD}$ [cm^2]	Double layer $ECSA_{cap}$ change [%]	Limiting current density j_{lim} (1600 rpm) [mA/cm^2]	Kinnetic current j_k [mA/cm^2]	e^- transfer coefficient n_{RRDE} [ ] at 0.6 V	e^- transfer coefficient n_{KL} [ ] at 0.6 V	Mass activity (1600 rpm) [A/mg]
1	W_xC - 700 °C	0.68	0.57	-	30	-2.80	0.41	-	2.1*	-
2	W_xC - 1100 °C	0.70	0.61	-	-23	-2.39	0.47	-	2.4*	-
3	W_xC - 1400 °C	0.76	0.65	-	3	-2.60	0.37	-	2.1*	-
4	W_xC - H_2 - 700 °C	0.76	0.66	-	3	-2.80	0.37	2.8	2.4*	-
5	W_xC - H_2 - 1100 °C	0.78	0.68	-	-1	-2.85	0.41	2.4	2.2*	-
6	W_xC - H_2 - 1400 °C	0.77	0.65	-	21	-2.70	0.47	2.8	2.3*	-
7	W_xC - 700 °C - Pt	0.88	0.60	-	-4	-2.34	0.51	3.3	2.4*	0.36
8	W_xC - 1100 °C - Pt	0.94	0.86	0.16	7	-5.65	0.17	3.98	4.1*	0.88
9	W_xC - 1400 °C - Pt	0.95	0.87	0.24	18	-5.81	0.16	4.0	5.8*	0.90
10	W_xC Pt	0.96	0.86	0.27	8	-5.76	0.18	3.95	4.1*	0.89
11	W_xC Pd	0.98	0.92	0.2**	27	-5.81	0.10	4.0	4.7*	1.61
12	W_xC Cu	0.75	0.64	-	0	-2.75	0.46	3.0	2.2*	1.02
13	W_xC Ag	0.81	0.68	-	12	-5.55	0.16	4.0	4.2*	1.76
14	GC Pt 40 nm	0.95	0.86	0.27	-	-5.65	0.17	-	4.3*	0.07
15	GC Pd 40 nm	0.95	0.86	0.53**	-	-5.81	0.3	-	4.6*	0.12
16	GC Cu 40 nm	0.73	0.62	-	-	-4.74	0.18	3.7	3.1*	0.13
17	GC Ag 40 nm	0.88	0.74	2.9**	-	-5.81	0.18	-	4.2*	0.14
18	GC 3nm Pt	0.96	0.89	0.16	10	-4.53	1.42			0.70
19	GC 3nm Pd	0.97	0.92	1.52**	1	-5.86	0.17	4.0	4.2*	1.62
20	GC 3nm Cu	0.71	0.60	-	18	-0.87	1.71	2.7	1.8*	0.32
21	GC 3nm Ag	0.82	0.65	-	0	-5.86	0.18	3.96	4.2*	1.86

Table 4.1: Performance characteristics of all presented samples. Some samples proved to give ambiguous or no results for some parts these are marked with '-'. Values marked with a * are values acquired through KL analysis, for this relies on the reaction to be one-step, one-way and first order, this has not been verified. Marked ** are values acquired through reduction peak measurements, with uncertain precision.

4.1.1 Annealed $\mathrm{W_xC}$ thin films

As discussed the sputtered W_xC thin films needed to be annealed after sputtering. Three different annealing temperatures were tested, (700, 1100 and 1400 °C). Sputtering W_xC resulted in a complex structured layer of W_xC, as can be seen in fig. 4.1. From the SEM (fig. 4.1) pictures of the sputtered W_xC layers different features are clearly available. Long nano-structures (in white), round shapes and a dark background. The white long nano-structures are likely graphitic carbon, the white round shapes are likely crystallised KOH left from the electrolyte during ORR, and the dark background is the W_xC. We can also note the difference in structure of the W_xC of the samples annealed at higher temperatures. The samples annealed at low temperatures show a meso-porous surface with pore size $\sim$ 20 nm and the samples annealed at higher temperatures show a more flake-like structure.

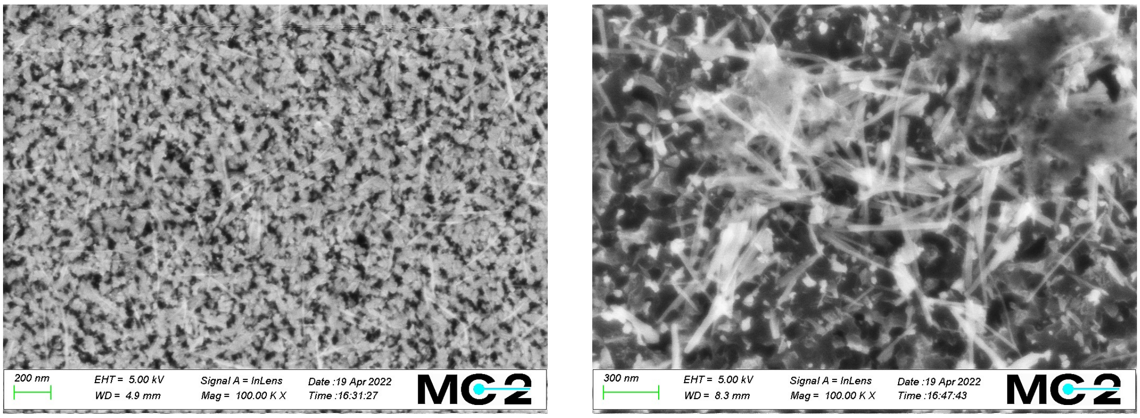

(a) 700 °C **(b)** 1100 °C

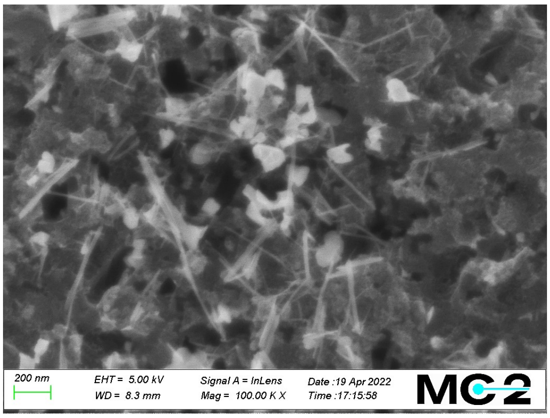

(c) 1400 °C

Figure 4.1: SEM picture taken of W_xC annealed at different temperatures *after* ORR measurement, noteable features are the straight nanostructures (probably graphite), white clumps of materials possibly crystalised KOH from measurements, and background of highly complex structured W_xC. Note that the brightness and contrast differs between the images and the W_xC appears more bright in (a).

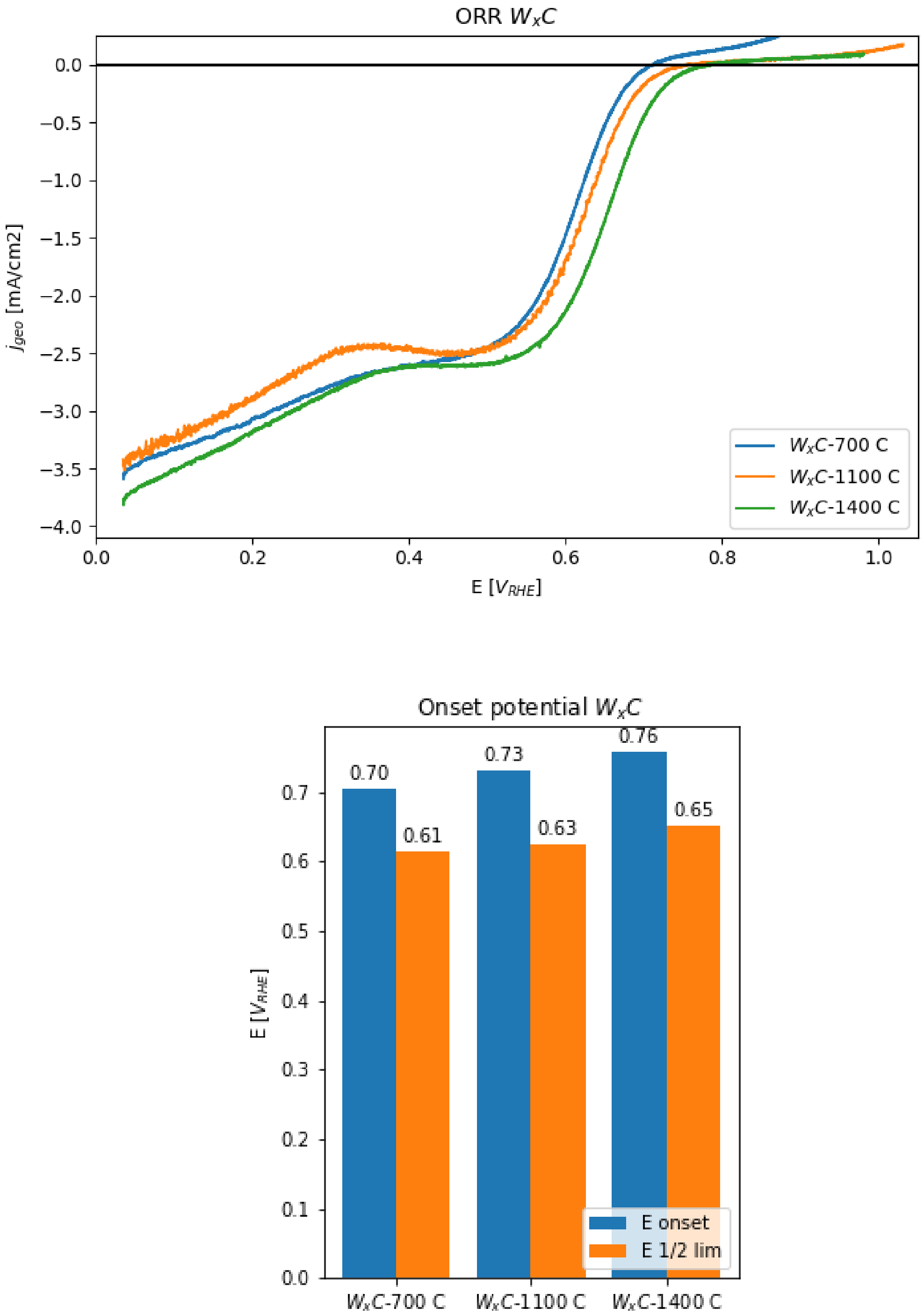

(a)

(b)

Figure 4.2: a) ORR result of samples (1-3) with W_xC annealed at different temperatures. b) E_O and $E_{1/2}$ for the different samples.

The ORR result of the samples can be seen in fig. 4.2a. The samples show a clear plateau in the current. This has been taken as the limiting current for the samples. At this current the reaction is not limited by the mass transport but is kinetically limited by the catalyst reactions.

4.1.2 Annealed + H_2 treated W_xC thin films

Following the annealing, samples were hydrogen treated. After H_2 treatment there were no more signs of graphitic carbon as can be seen in the SEM pictures taken fig. 4.5. Thus the H_2 treatment has removed the graphitic carbon on the surface.
It is also clear that the morphology of the surface changes during the ORR measurement fig. 4.5. This is noteworthy since the morphology is tightly bound to the ECSA and for these samples the capacitive current change is only a few percent table 4.1. The change in morphology is also different for the different annealing temperatures. It is possible this is because the different annealing temperatures result in different ratios of the phases of WC.
The ORR polarisation curves for the $W_xC + H_2$ samples are seen in fig. 4.3a. The W_xC-H_2 has a slightly better performance than the other two samples, both in terms of potential and current. For this sample too, the reaction is not kinetically limited.

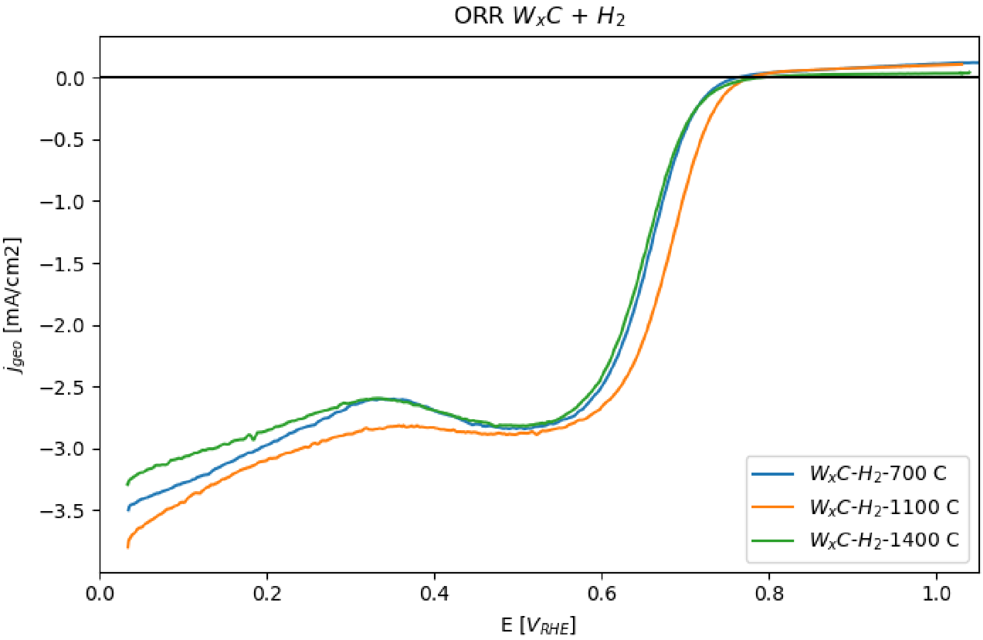

(a)

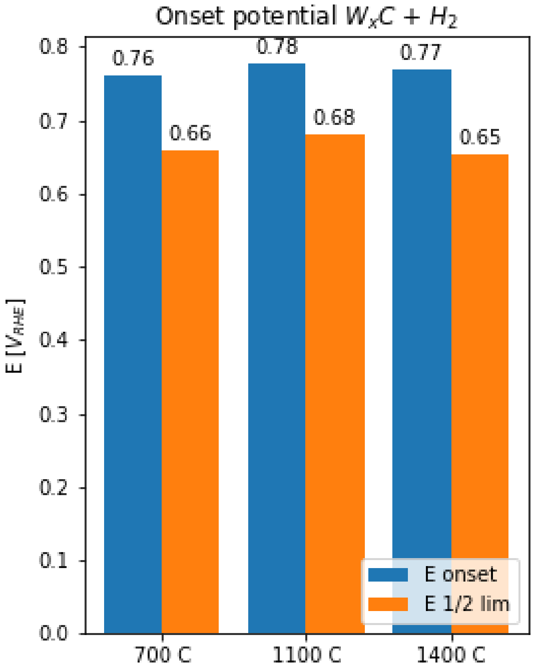

(b)

Figure 4.3: a) ORR result of samples (4-6) W_xC + H_2 annealed at different temperatures and H_2 treated b) E_O and $E_{1/2}$ for the different samples.

4.1.3 Pt 3 nm evaporated on $\mathrm{W_xC}$ annealed at different temperatures

Finaly samples were fabricated with W_xC after H_2 treatment and with 3 nm of Pt, corresponding ORR polarisation curves can be seen in fig. 4.4. The data shows that the samples annealed at 1400 °C, had the best onset potential and limiting current. The W_xC 1100 °C Pt and W_xC 1400 °C Pt have very similar onset potential yet W_xC 1400 °C Pt is slightly better. The Pt 700 °C does not show any Pt activity in the ORR polarisation curve, likely because all Pt has fallen off already at the start. 1400 °C was therefore deemed to be the most appropriate annealing temperature.

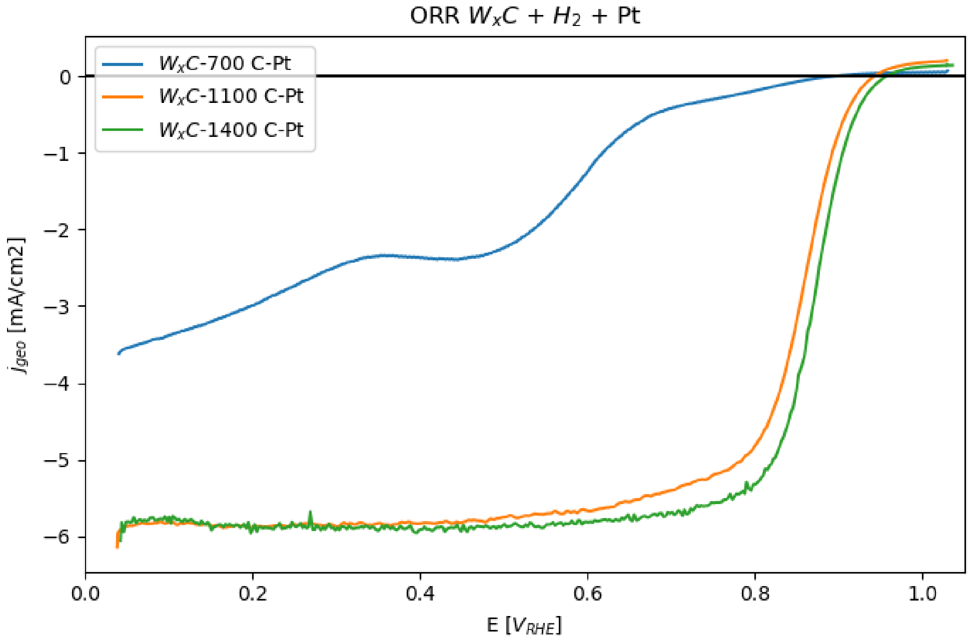

(a)

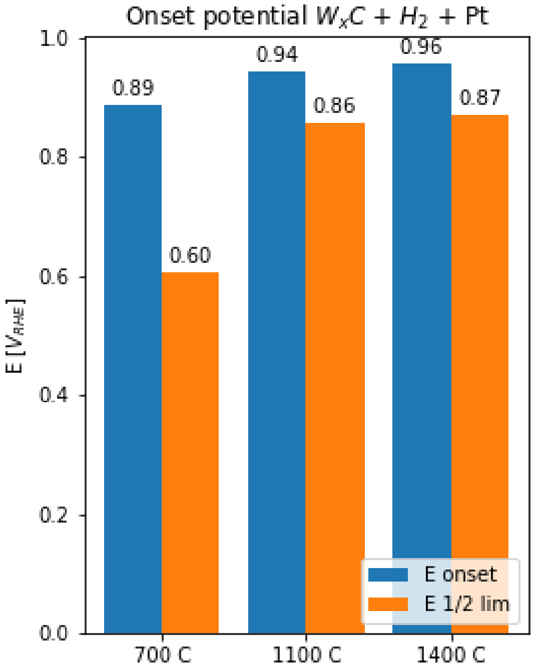

(b)

Figure 4.4: a) ORR result of samples (7 - 9) W_xC + H_2 + Pt 3 nm annealed at different temperatures b) E_O and $E_{1/2}$ for the different samples.

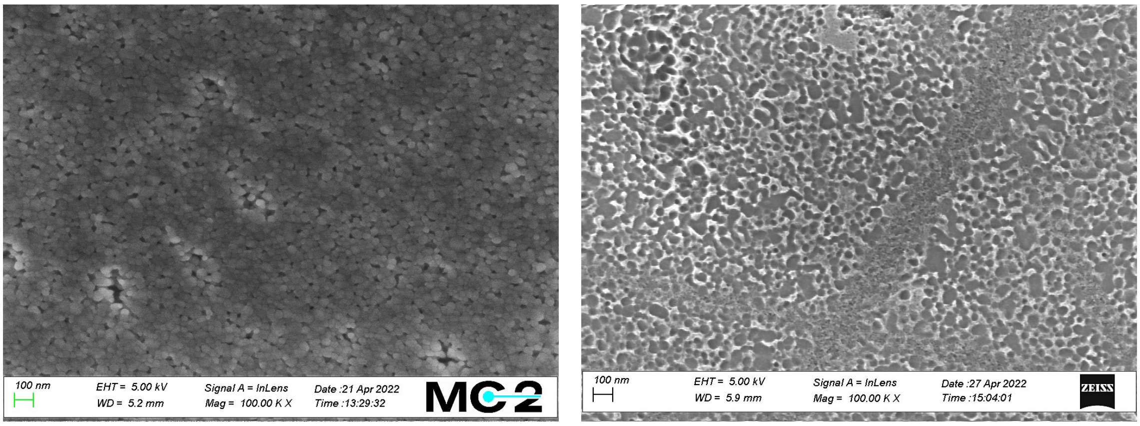

(a) 700 °C before ORR **(b)** 700 °C after ORR

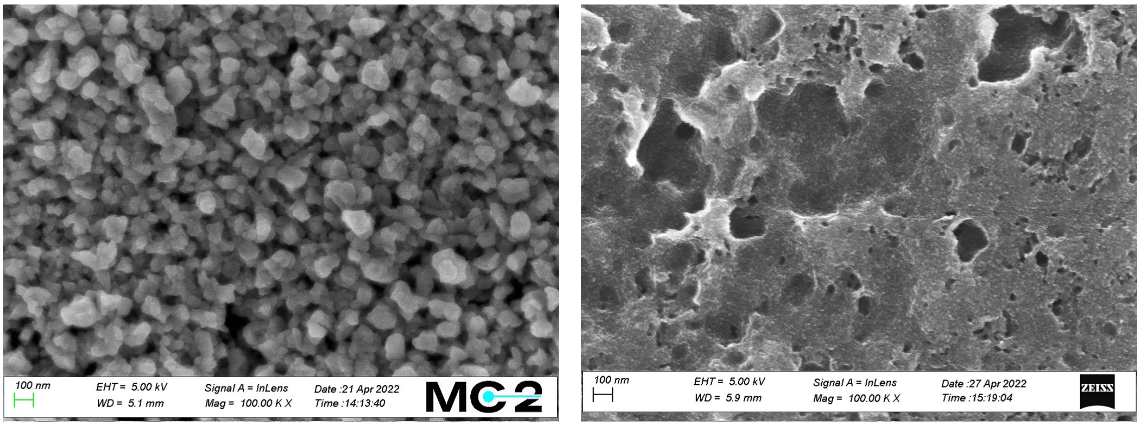

(c) 1100 °C before ORR **(d)** 1100 °C after ORR

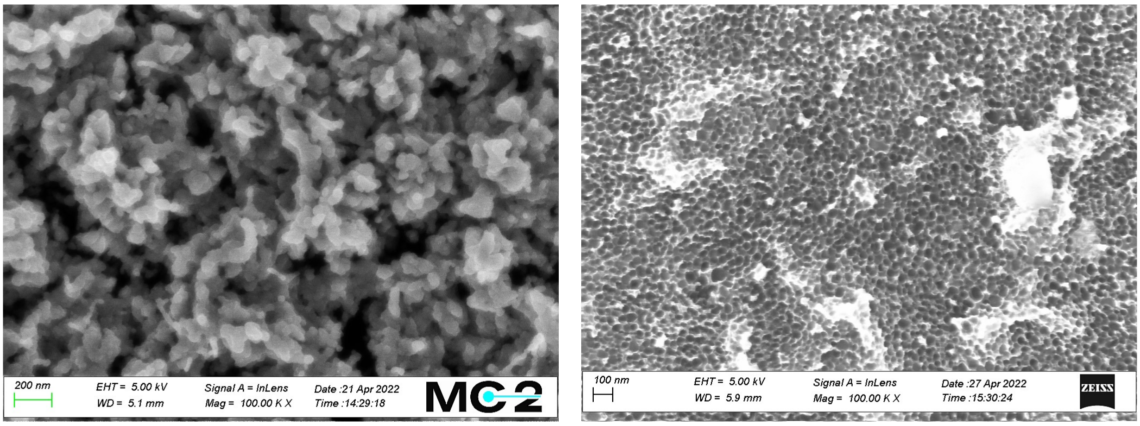

(e) 1400 °C before ORR **(f)** 1400 °C after ORR

Figure 4.5: SEM pictures taken of samples (4 - 6) $W_xC + H_2$ annealed at different temperatures and H_2 treated before and after ORR measurement,

4.2 ECSA measurements

Two different methods were used to study the ECSA as described in section 2.1.4 and section 2.1.5. Both methods were carried out before and after the ORR measurement in order to study any change taking place during measurement. Ideally one would want to use the same method for all samples, to get the ECSA. This, however, is not possible since the $\mathrm{H_{UPD}}$ peak of Pt is does not exist for the other elements. Instead reduction peaks can be measured but with reduced accuracy. Therefore the capacitance method need to be used which in the greatly reduce the reliability when comparing between different methods.

4.2.1 $\mathbf{H_{UPD}}$ ECSA measurements

The $\mathrm{H_{UPD}}$ is the most reliable way of measuring the ECSA of Pt electrocatalyst. However, there still exists some caveat regarding this method as well.

First of all, the measurement only takes into account the surface area of Pt. Since in the substrate W_xC is very porous it is plausible that the total surface area is affected not only by the surface area of Pt but also by the area of W_xC. It is uncertain to what extent the substrate is covered by the catalyst. The underlying quantity that is being measured might therefore be completely different than the quantity measured in $ECSA_{CAP}$ which makes comparisons uncertain.

The major issue for measuring the $ECSA_{HUPD}$ has been the absence of the $\mathrm{H_{UPD}}$ peak. As can be seen in fig. 4.6 the $\mathrm{H_{UPD}}$ peak is almost non-existant before the ORR measurement and much larger after. This peak before is so small that it is not visible on the slope of the hydrogen evolution peak, making the method unable to give a good result for $ECSA_{HUPD}$. Two possible explanations for this is

1. The $ECSA_{HUPD}$ changes a lot during the ORR measurement. If the $ECSA_{HUPD}$ were small before and turned much larger during the process this would lead to a big increase in the $\mathrm{H_{UPD}}$ peak. However fig. 4.5 does not show any such progress. A reduction in $ECSA_{HUPD}$ would also be in agreement with the reduction of interfacial energy.

2. If the Pt is hidden deep in the surface during sputtering then it is not accessible for the H_2 molecules. It is then possible during the ORR measurement that the oxidation/reduction of the surface changes the surface structure to push more Pt to the surface. This would explain the increase in $\mathrm{H_{UPD}}$. This could happen either through lattice migration or through dissolving the W_xC not covered by Pt. If W_xC is dissolving this would likely also cause Pt to fall of as well which would be bad for the stability of the catalyst.

Since the $ECSA_{HUPD}$ changes so much during the ORR the reported $ECSA_{HUPD}$ will be the one measured after ORR.

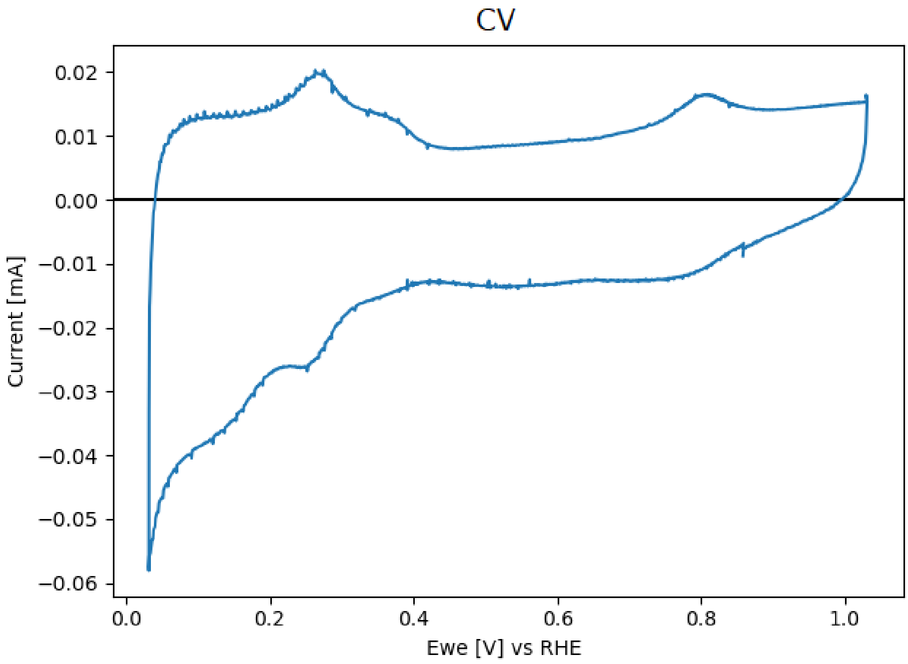

(a) Before ORR

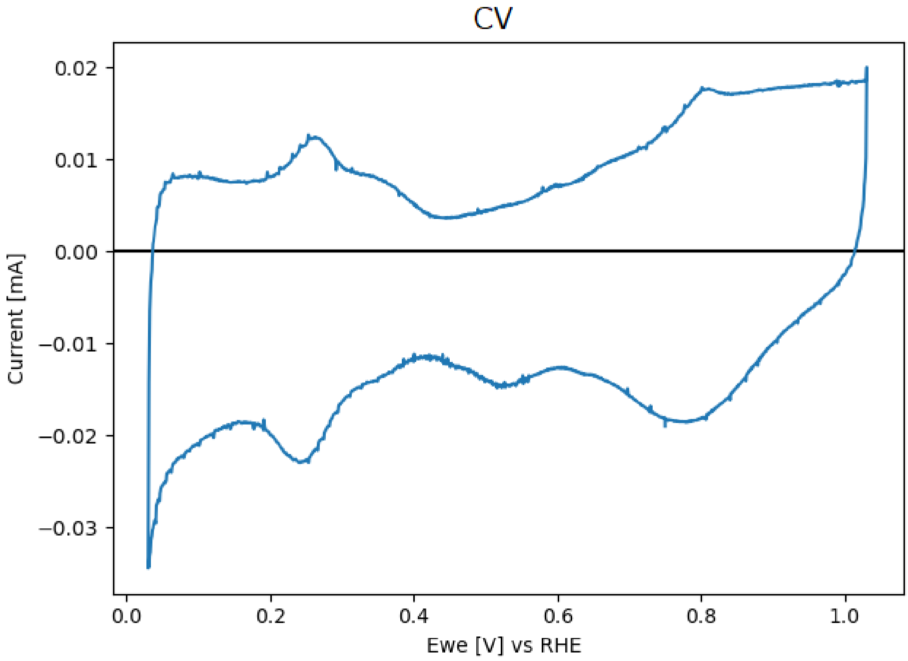

(b) After ORR

Figure 4.6: Showing the CV to measure H_{UPD} before and after ORR. Note how there is almost no visible H_{UPD} before ORR measurement and a clear peak after.

4.2.2 Reduction peak ECSA measurements

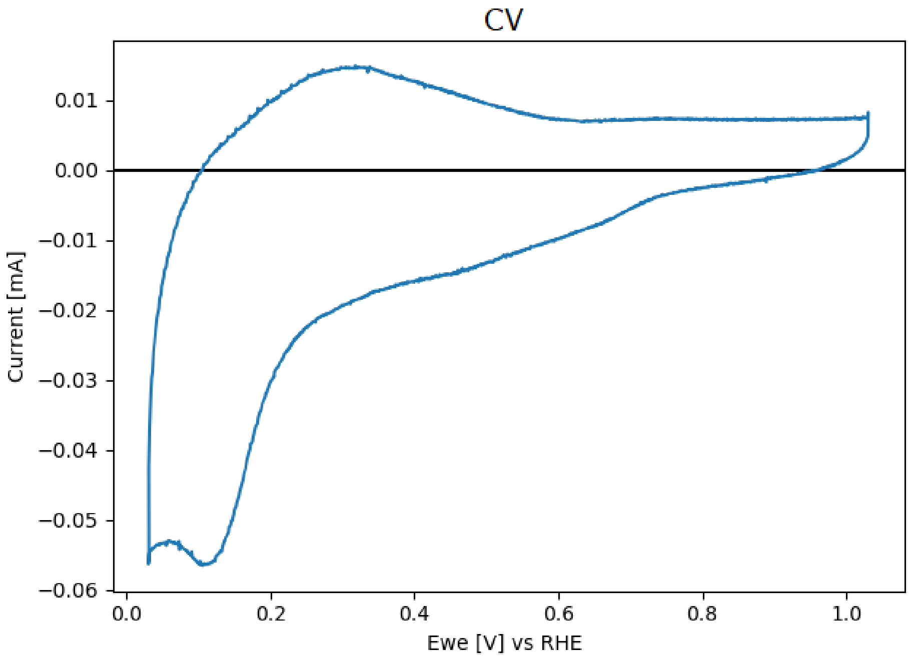

(a) W_xC Cu

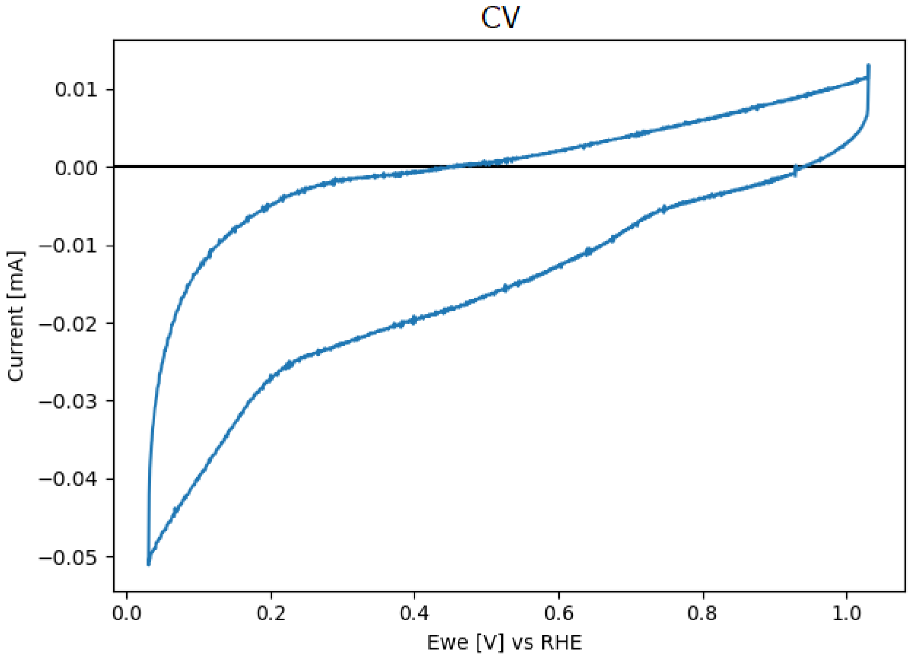

(b) W_xC Ag

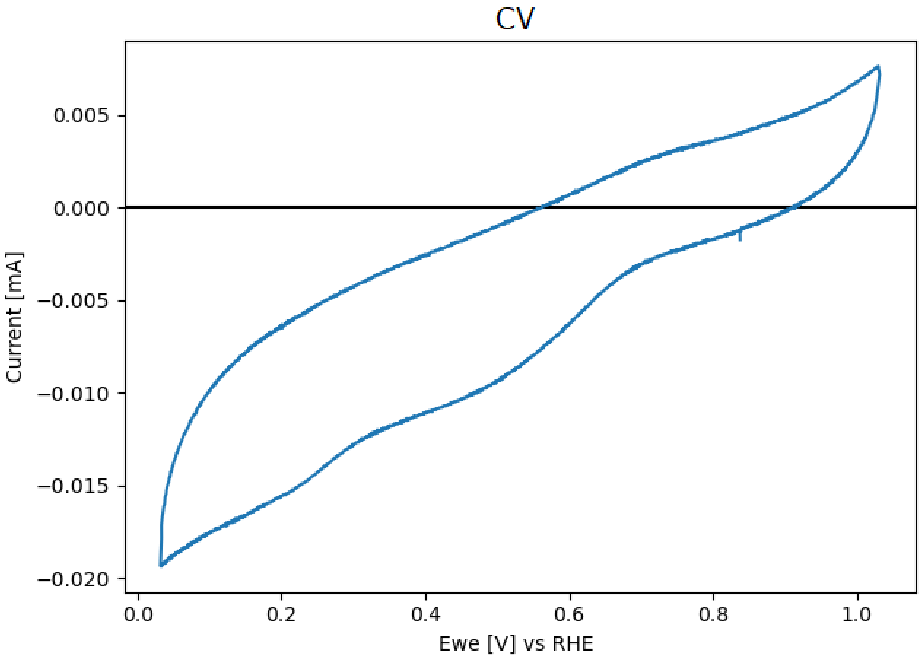

(c) GC 3 nm Cu

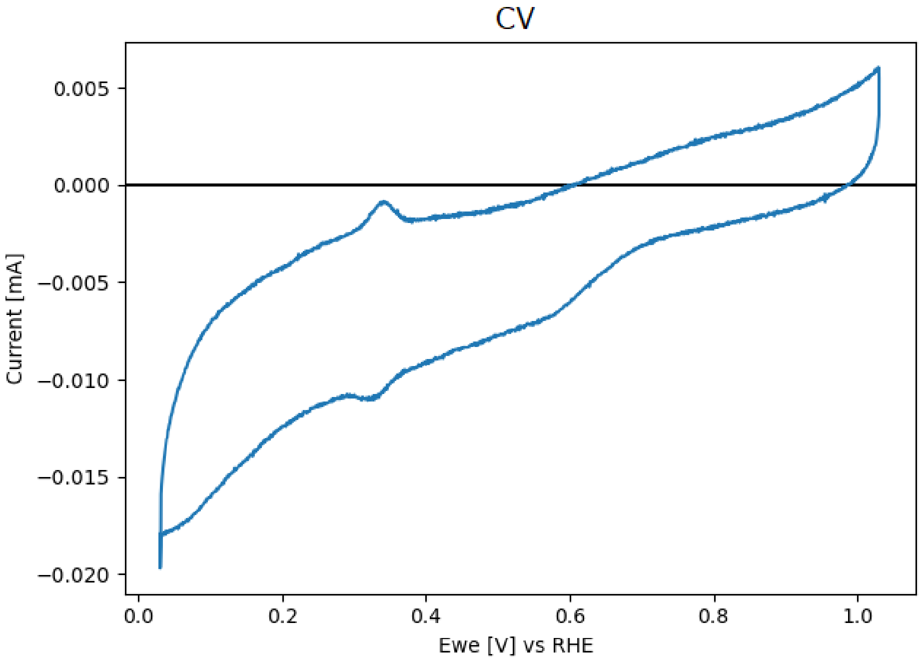

(d) GC 3 nm Ag

Figure 4.7: CVs of samples (12, 13, 20, 21), before ORR measurements. No reduction peaks are visible.

Reduction peak measurements of the ECSA are carried out in a very similar fashion to the H_{UPD} peak but the integrated charge peak is instead the one corresponding to the reduction of a surface monolayer. This has a wider application since the oxidation/reduction features of many elements are visible within the potential range at which the CVs were recorded. Many attempts were made to elucidate the ECSA for the samples with Cu and Ag. However for the very thin films of Cu and Ag samples (Nr: 12, 13, 20, 21) there no peaks were measurable (see fig. 4.7). Thus the $ECSA_{red}$ of these samples could not be found. For the Pd sample there is a reduction peak giving a value for the $ECSA_{red}$.

4.2.3 Capacitive ECSA measurements

This method has a large uncertainty because of the strong direct influence of a range of factors such as the specific capacitance, the uncertainty of isolating the capacitive current i_{cap} and the strong dependence on what elements are being studied. Because of all of these shortcomings the method is only used to study the change of the ECSA before and after ORR measurements. In this way the most of the sources of error can be estimated to be at least the same before and after. However some sources of error still persist such as the effect of different oxidation states before and after. To isolate all of these effects are outside of what is deemed feasible for this study, Therefore the accuracy of the acquired $ECSA_{CAP}$ is low but we conclude that, as long as these measurements are carried out in a systematic way, we can use this method to track the change in ECSA through electrochemical evaluation.

4.3 Metals evaporated on W_xC-1400-H_2

To make comparison with similar studies the results are presented as geometric currents. As there has been little succes in measuring the ECSA in a satisfactory way, the current reported will be vs the geometric area.

4.3.1 Pt 3nm/W_xC

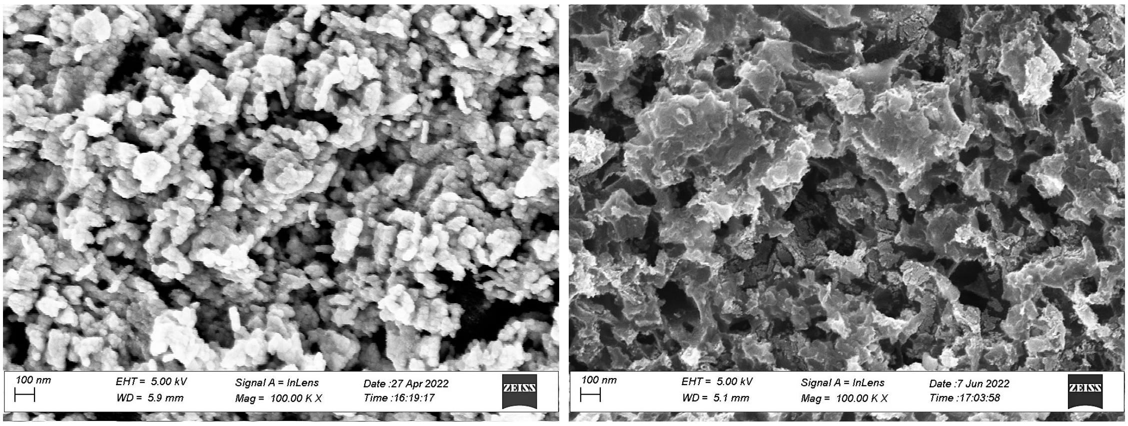

(a) Before ORR **(b)** After ORR

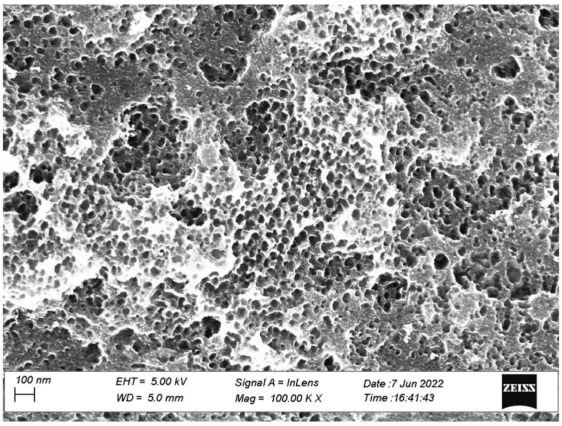

(c) After 2000 cycles ORR

Figure 4.8: SEM picture of Sample 10 before and after ORR measurements, as well as after 2000 cycles of ORR.

As can be seen in fig. 4.9a sample Nr 10 with 3 nm of Pt performs as good as the sample with 40 nm of Pt. For W_xC this means a very good mass activity, of 0.89 A/mg Pt. This also performs much better than commercially available Pt with specific activity of 0.2 A/mg Pt[26]. The sample GC 3 nm Pt initially shows the same mass activity but after only a few cycles the electrochemical behaviour shows a clear of degradation. This result strongly supports the hypothesis of W_xC being a good support catalyst support. The electron transfer coefficient is very close to 4 for both measurements see table 4.1. This is a significant result meaning that the reaction is almost entirely dominated by the 4 electron pathway.

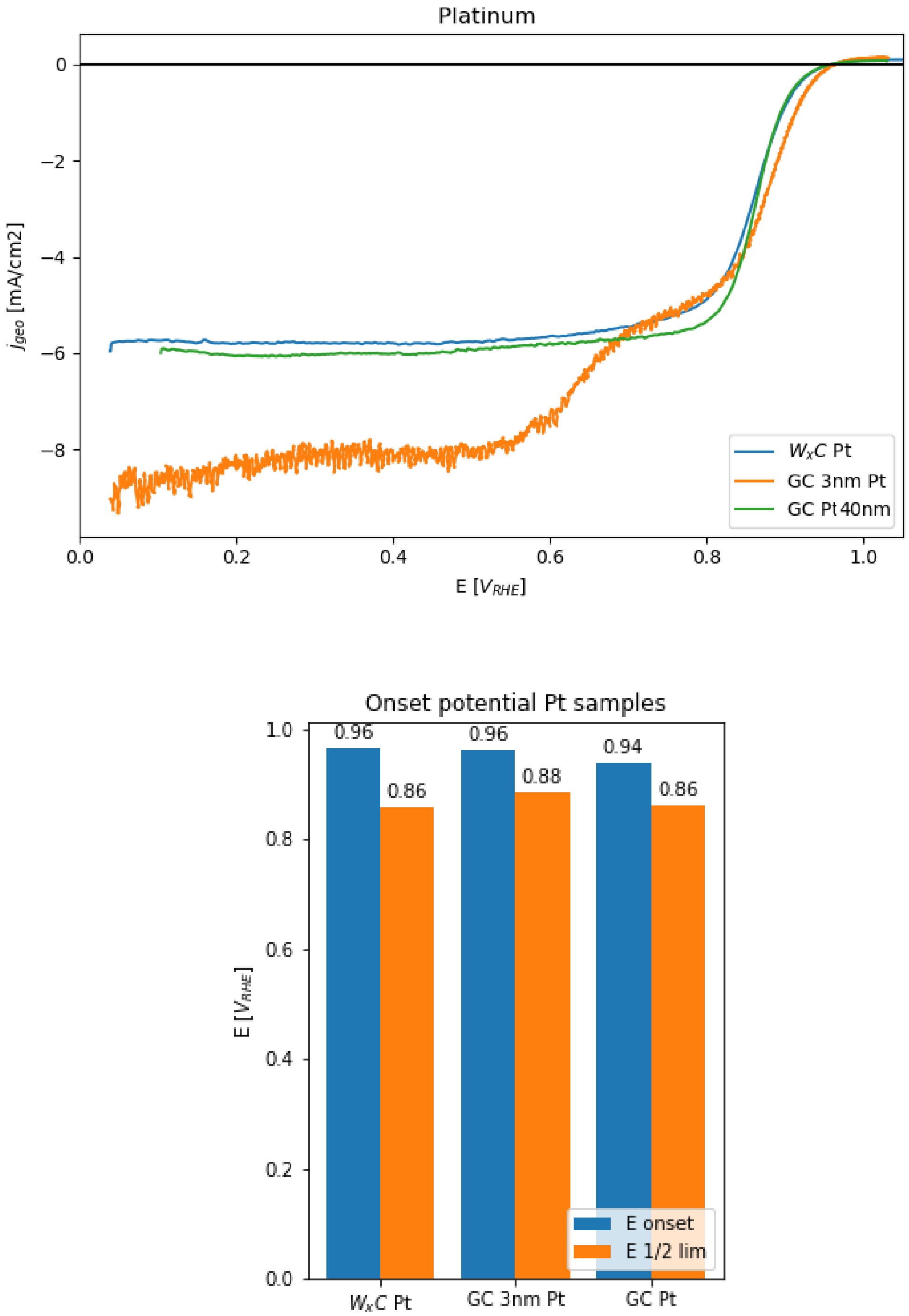

(a)

(b)

Figure 4.9: a)ORR polarisation curves for different thicknesses of Pt (samples 10, 14, 18) b) E_O and $E_{1/2}$ for the samples, The very high current for GC 3nm Pt is above what is possible for mass transfer, meaning the current does not only stem from the ORR reaction.

4.3.2 Pt on W_xC stability

In order to further test the hypothesis of W_xC as support, a long cycling test was performed on sample 10. This entailed cycling it 2000 times, over a period of about 22 hours. The development of the catalyst activity can be seen in fig. 4.10. From this it is clear that the activity of Pt with W_xC as support is not impeded by 2000 cycles of catalytic activity. This is promising for the possibility of another leap in Pt reduction on FC catalysts. During the measurement there is also a clear increase in E_o and $E_{1/2}$, this is also a very promising feature for FC catalyst.

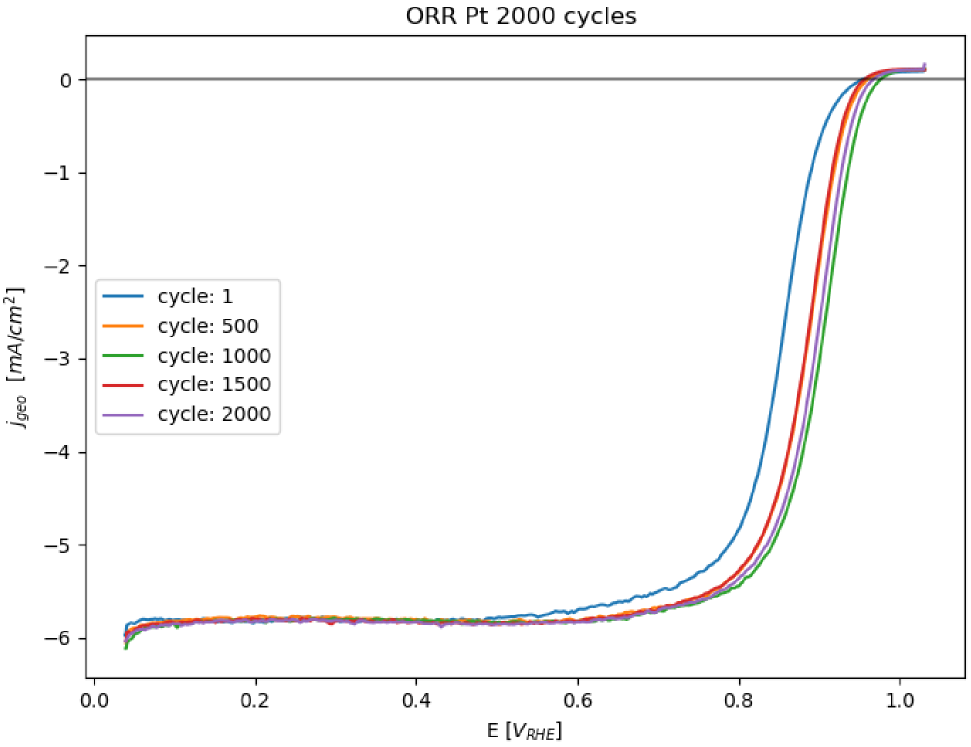

Figure 4.10: ORR polarisation result for W_xC Pt long measurement. Plotted curves every 500 cycles.

Studying the SEM images after 2000 cycles there is a clear change in the surface after many cycles. After a few cycles the Pt clusters of ∼20 nm are no longer present and after many cycles holes are appearing on the surface. This might indicate that there is damage to the W_xC during long term O2 measurement. It is also possible that Pt has alloyed itself with W_xC during ORR cycling which could increase the activity and stability of the catalyst.

To further investigate the stability a much longer test of 1000+ hours would be needed as well as accelerated stress testing (AST), to simulate real-life conditions and provide necessary data that helps ensure the catalyst stability.

4.3.3 Pd 3nm/W_xC

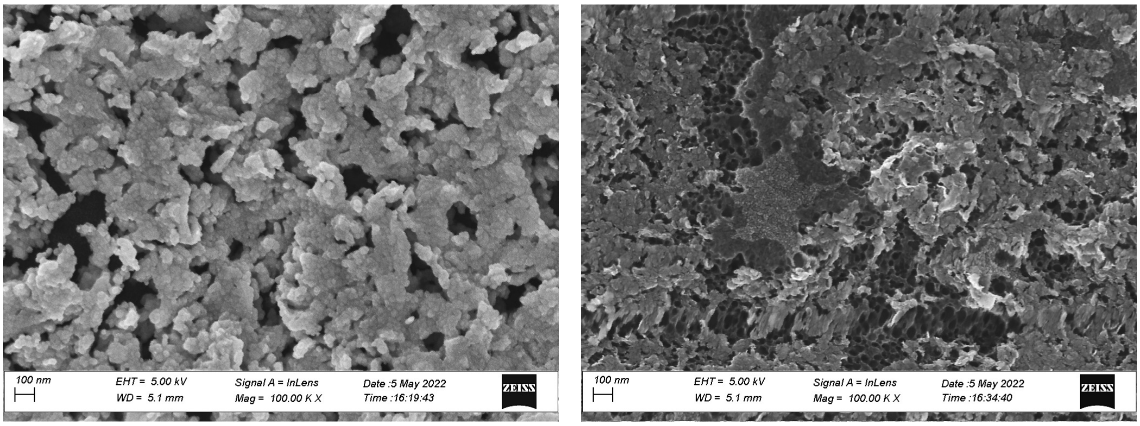

(a) Before ORR **(b)** After ORR

Figure 4.11: SEM picture of Sample 11 before and after ORR measurements.

As expected, Pd as catalytic material also showed very good activity fig. 4.12a. The half max potential of the W_xC Pd catalyst even exceeds that of GC Pd 40 nm. The onset potential however is very similar and therefore the higher activity is possibly explained by a higher ECSA, because the W_xC support has a higher porosity than GC. The E_o and $E_{1/2}$ are even better than Pt on W_xC indicating a good catalyst table 4.1.

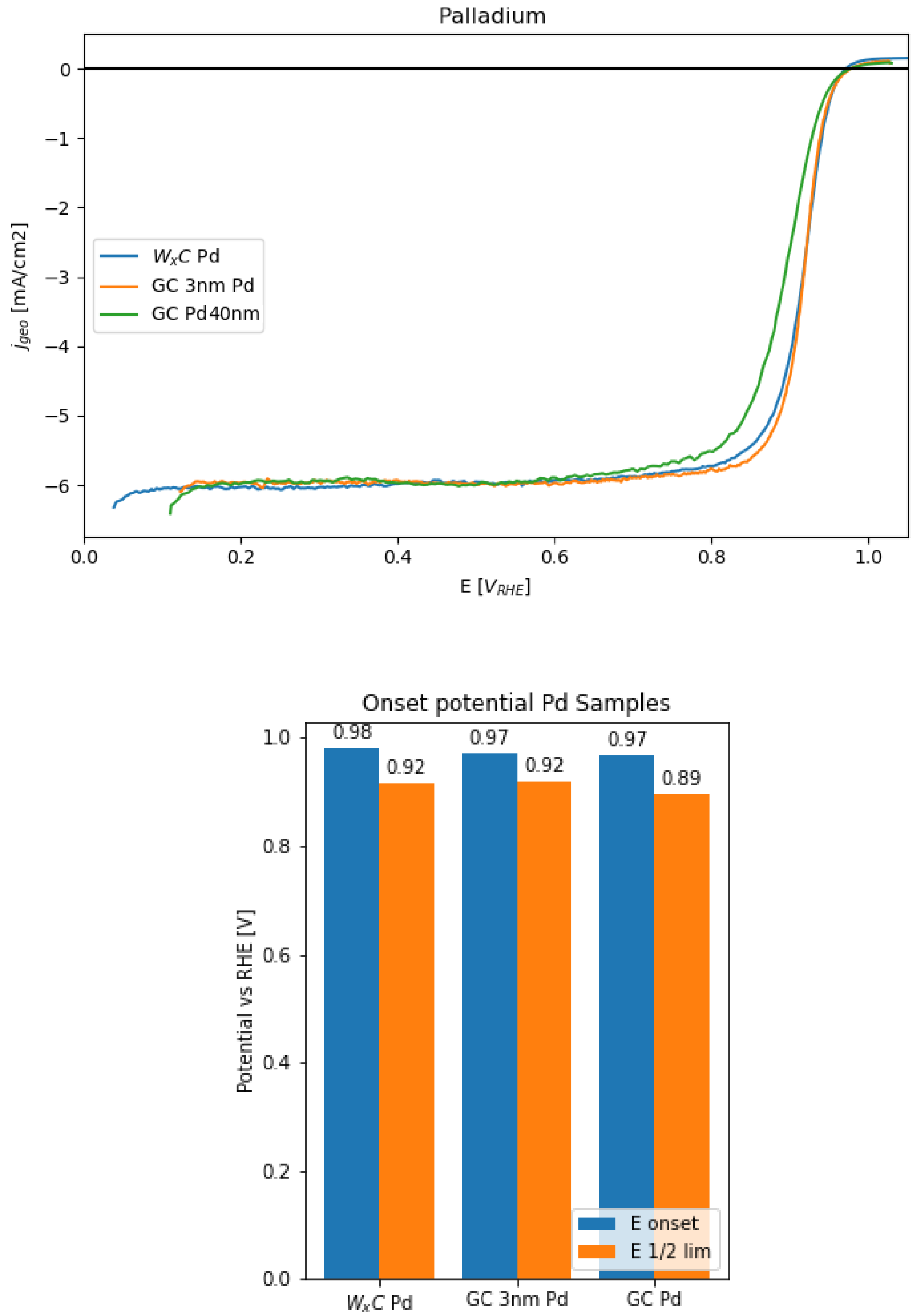

(a)

(b)

Figure 4.12: a) ORR measurement results for different thicknesses of Pd (samples 11, 15, 19) b) E_O and $E_{1/2}$ for the samples.

The electron transfer coefficient n_{RRDE} of 4 indicate a 4e dominated reaction. The $n_{KL} = 4.7$ is not possible indicating that the conditions for the Koutecký-levich analysis are not met [5]. The mass activity of W_xC 1.61 A/mg (table 4.1) would also be a considerable improvement if it can be showed to be stable catalyst. This should not be compared to the mass activity of W_xC Pt however as the density of Pd is almost half that of Pt. No long duration test has been done for the Pd catalysts, this is necessary to ensure it is a durable catalyst.

4.3.4 Cu 3nm/$\mathrm{W_xC}$

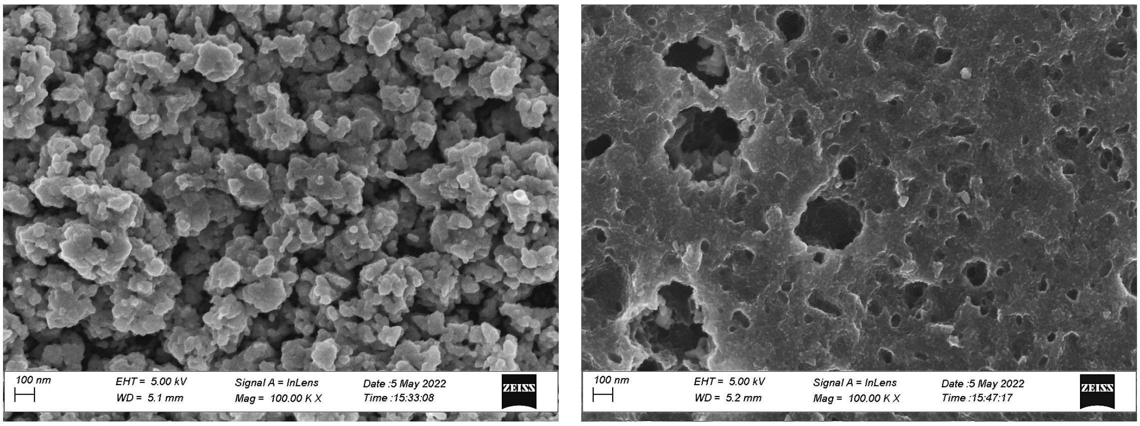

(a) Before ORR **(b)** After ORR

Figure 4.13: SEM picture of Sample 12 before and after ORR measurements.

The onset potential fig. 4.14a for Cu is rather low. The onset potential of W_xC Cu is the same as Cu which indicates no strong alloying or lattice effect. The ORR curve also indicate that the reaction is not mass transport limited as the current increases higher overpotentials in fig. 4.14a. Indicating a poor catalyst. The SEM images fig. 4.13 also indicate a complete change of the catalyst surface after ORR measurement. Comparing the ORR polarisation curve of W_xC Cu with W_xC + H_2 fig. 4.3a, reveales that these are almost identical, indicating that the Cu has detached from the surface. Because Cu is unable to stay on support no conclusion can be drawn on its catalytic capability. However the stability issues mean Cu on W_xC does not seem a fruitful catalyst.

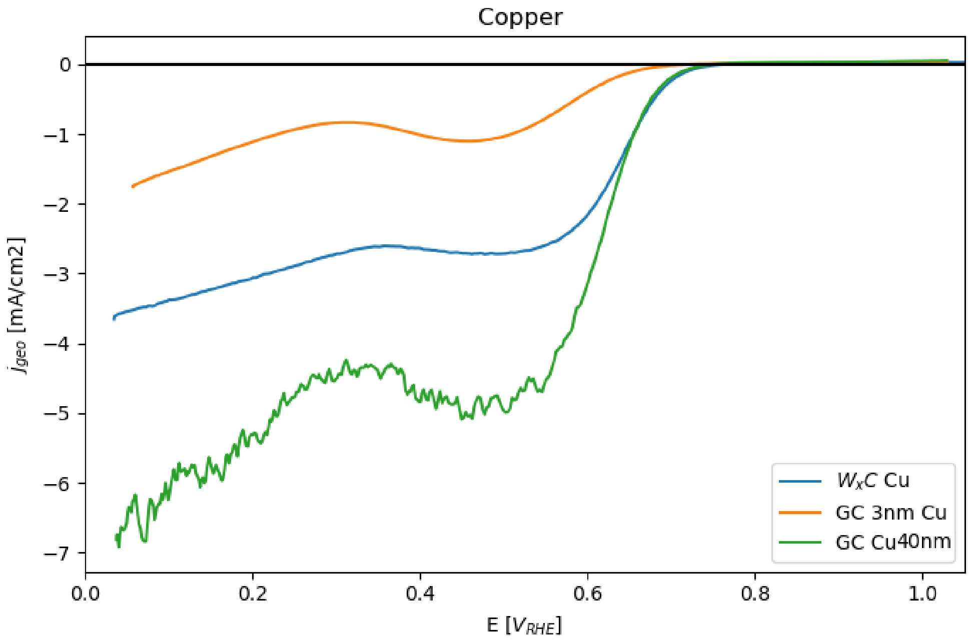

(a)

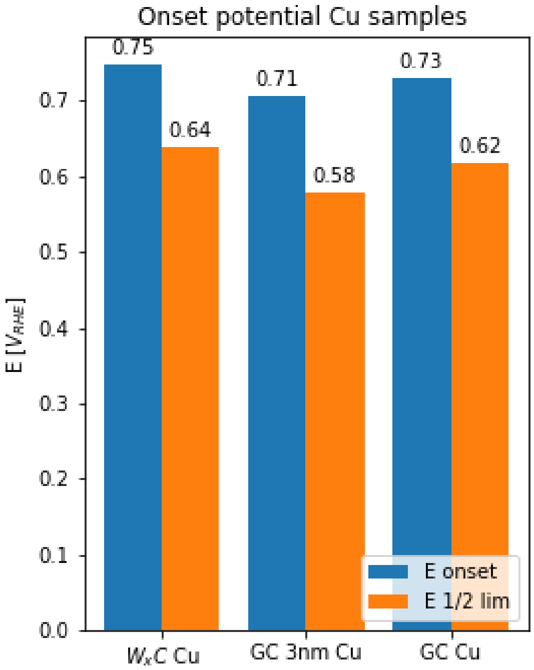

(b)

Figure 4.14: a) ORR measurement results for different thicknesses of Cu (samples 12, 16, 20) b) E_O and $E_{1/2}$ for the samples.

4.3.5 Ag 3nm/$\mathrm{W_xC}$

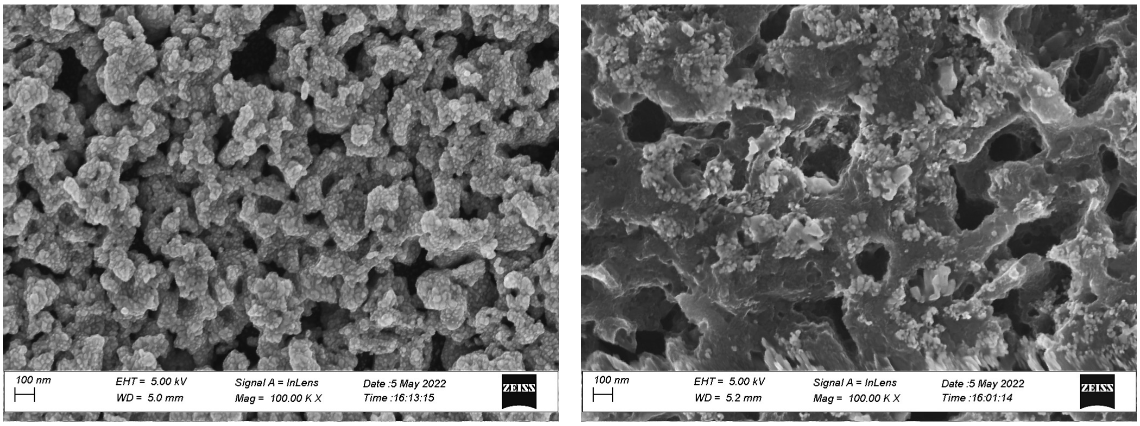

(a) Before ORR **(b)** After ORR

Figure 4.15: SEM picture of Sample 13 before and after ORR measurements.

The ORR onset potential of Ag on W_xC is considerably worse than pure GC Ag 40 nm, as seen in fig. 4.16a. Clearly W_xC does not improve the catalytic ability of the silver. The limiting reaction in fig. 4.16a is strongly mass transport limited. This means that even though W_xC Ag has a high overpotential the reaction rate at that potential is high. The e^- transfer coefficient shows the reaction way is almost entirely the 4e pathway.

In the images of the W_xC Ag there is some indication that the Ag does not adhere well enough to the surface either fig. 4.15. Although not as apparent as Cu, studying the SEM images, a lot of the Ag appears to have detached from the surface.

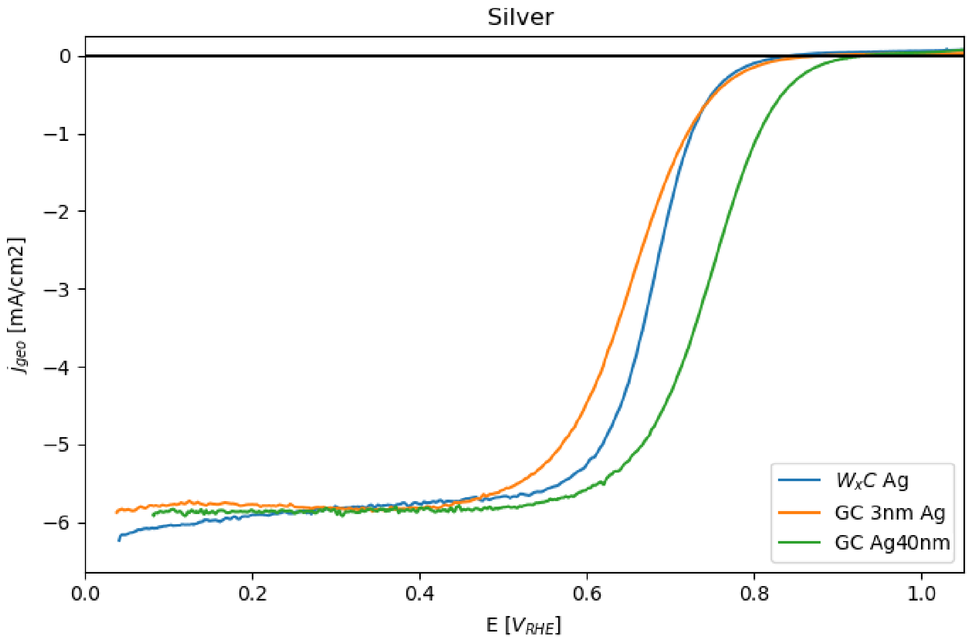

(a)

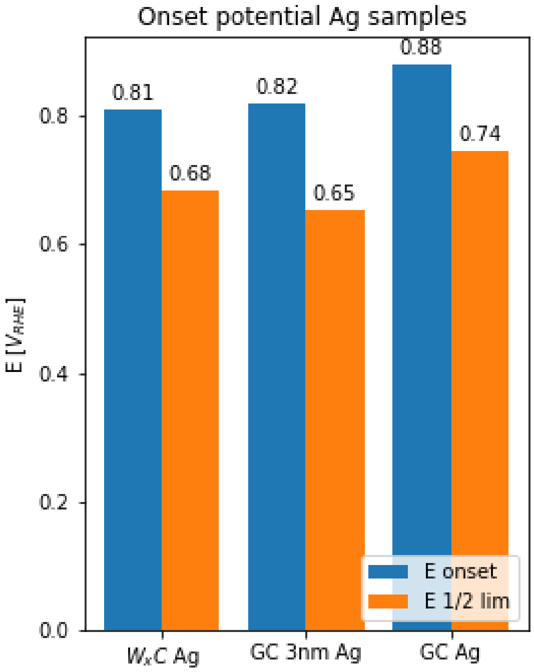

(b)

Figure 4.16: a) ORR measurement results for different thicknesses of Ag (samples 13, 17, 21) b) E_O and $E_{1/2}$ for the samples.

5

Conclusion

W_xC thin films have been fabricated and parameters for a suitable fabrication have been identified. On the substrate catalytic layers have been added in order to test their aptness with W_xC as support. Ag and Cu show poor catalytic result compared to their 40 nm references as well as bad adherence. On the other hand, Pt and Pd show very good results even at extremely low PGM loadings. The onset and half wave potential is on par with and sometimes even better than the reference Pt. For these catalyst the reaction pathway is almost entirely through the 4 electron pathway and the samples are more stable than samples without W_xC support. With further confirmation it is possible that the W_xC supported catalysts enables MEAs with significantly lower PGM loading than today's technology.

Bibliography

[1] Thomas Earl et al. “Analysis of long haul battery electric trucks in EU Marketplace and technology, economic, environmental, and policy perspectives. European Federation for Transport and Environment”. In: (2018), pp. 17–18. URL: `https://ec.europa.eu/inea/en/ten-t/ten-t-projects`.

[2] Andrew L. Dicks and David A. J. Rand. “Fuel Cell Systems Explained”. In: *Fuel Cell Systems Explained* (Apr. 2018). DOI: `10.1002/9781118706992`. URL: `https://onlinelibrary.wiley.com/doi/book/10.1002/9781118706992`.

[3] Xiaoming Ge et al. “Oxygen Reduction in Alkaline Media: From Mechanisms to Recent Advances of Catalysts”. In: *ACS Catalysis* 5 (8 Aug. 2015), pp. 4643–4667. ISSN: 21555435. DOI: `10.1021/ACSCATAL.5B00524/ASSET/IMAGES/LARGE/CS-2015-005246_0016.JPEG`. URL: `https://pubs.acs.org/doi/full/10.1021/acscatal.5b00524`.

[4] Minoru Inaba et al. “Gas crossover and membrane degradation in polymer electrolyte fuel cells”. In: *Electrochimica Acta* 51 (26 Aug. 2006), pp. 5746–5753. ISSN: 00134686. DOI: `10.1016/j.electacta.2006.03.008`.

[5] Ruifeng Zhou et al. “Determination of the Electron Transfer Number for the Oxygen Reduction Reaction: From Theory to Experiment”. In: (2016). DOI: `10.1021/acscatal.6b01581`. URL: `https://pubs.acs.org/sharingguidelines`.

[6] Nagappan Ramaswamy and Sanjeev Mukerjee. “Fundamental mechanistic understanding of electrocatalysis of oxygen reduction on Pt and non-Pt surfaces: Acid versus alkaline media”. In: *Advances in Physical Chemistry* 2012 (2012). ISSN: 16877985. DOI: `10.1155/2012/491604`.

[7] T. B. Ferriday and Peter Hugh Middleton. “Alkaline fuel cell technology - A review”. In: *International Journal of Hydrogen Energy* 46 (35 May 2021), pp. 18489–18510. ISSN: 0360-3199. DOI: `10.1016/J.IJHYDENE.2021.02.203`.

[8] R. B. Levy and M. Boudart. “Platinum-Like Behavior of Tungsten Carbide in Surface Catalysis”. In: *Science, New Series* 181 (1973), pp. 547–549. URL: `https://www.jstor.org/stable/1736506?seq=1#metadata_info_tab_contents`.

[9] V. Sh Palanker et al. “Catalytic activity and capacitance of tungsten carbide as a function of its dispersity and surface state”. In: *Electrochimica Acta* 22 (6 June 1977), pp. 661–667. ISSN: 0013-4686. DOI: `10.1016/0013-4686(77)85136-0`.

[10] Andrew Hamnett Wolf Vielstich Carl H. Hamann. *Electrochemistry, 2nd, Completely Revised and Updated Edition.* 2007, p. 550. ISBN: 978-3-527-31069-2. URL: `https://www.wiley.com/en-us/9783527310692%20https://www.wiley.com/en-us/Electrochemistry%5C%2C+2nd%5C%2C+Completely+Revised+and+Updated+Edition-p-9783527310692`.

[11] Craig E Banks Richard Guy Compton. *Understanding Voltammetry (Third Edition)).* Aug. 2018. ISBN: 9781786345295. URL: `https://www.bokus.com/bok/9781786345295/understanding-voltammetry-third-edition/?gclid=CjwKCAjw7IeUBhBbEiwADhiEMTgLsU4poq1KUv2T1BdANbhBWoa1jYdQSsk4_2TFeBx4co6GBSwUOxoC5xkQAvD_BwE`.

[12] Biologic. *What is Electrochemical Impedance Spectroscopy (EIS)? (Electrochemistry Basics Series) - Biologic.* Mar. 2022. URL: `https://www.biologic.net/topics/what-is-eis/`.

[13] Paula Connor et al. “The Determination of Electrochemical Active Surface Area and Specific Capacity Revisited for the System MnOx as an Oxygen Evolution Catalyst”. In: *Zeitschrift fur Physikalische Chemie* 234 (5 May 2020), pp. 979–994. ISSN: 09429352. DOI: `10.1515/ZPCH-2019-1514/DOWNLOADASSET/SUPPL/ZPCH-2019-1514_SUPPL.DOCX`. URL: `https://www.degruyter.com/document/doi/10.1515/zpch-2019-1514/html`.

[14] S. Trasatti and O. A. Petrii. “International Union of Pure and Applied Chemistry Physical Chemistry Division Commission on Electrochemistry: Real Surface Area Measurements in Electrochemistry”. In: *Pure and Applied Chemistry* 63 (5 Jan. 1991), pp. 711–734. ISSN: 13653075. DOI: `10.1351/PAC199163050711/MACHINEREADABLECITATION/RIS`. URL: `https://www.degruyter.com/document/doi/10.1351/pac199163050711/html`.

[15] Silvia Duran et al. “Electrochemical Active Surface Area Determination of Iridium-Based Mixed Oxides by Mercury Underpotential Deposition”. In: *ChemElectroChem* 8 (18 Sept. 2021), pp. 3519–3524. ISSN: 2196-0216. DOI: `10.1002/CELC.202100649`. URL: `https://onlinelibrary.wiley.com/doi/full/10.1002/celc.202100649%20https://onlinelibrary.wiley.com/doi/abs/10.1002/celc.202100649%20https://chemistry-europe.onlinelibrary.wiley.com/doi/full/10.1002/celc.202100649?saml_referrer=`.

[16] Justus Masa et al. “Koutecky-Levich analysis applied to nanoparticle modified rotating disk electrodes: Electrocatalysis or misinterpretation”. In: *Nano Research 2014 7:1* 7 (1 Oct. 2013), pp. 71–78. ISSN: 1998-0000. DOI: `10.1007/S12274-013-0372-0`. URL: `https://link.springer.com/article/10.1007/s12274-013-0372-0`.

[17] Gerard M. Sisó. “Electrocatalyst materials for low-temperature hydrogen fuel cells”. Chalmers, 2021. URL: `https://research.chalmers.se/en/publication/523045`.

[18] Wikipedia. *Abundance of elements in Earth’s crust — Wikipedia, The Free Encyclopedia.* `http://en.wikipedia.org/w/index.php?title=Abundance%20of%20elements%20in%20Earth's%20crust&oldid=1078611905`. [Online; accessed 24-May-2022]. 2022.

[19] Wikipedia. *Sputter deposition — Wikipedia, The Free Encyclopedia.* `http://en.wikipedia.org/w/index.php?title=Sputter%20deposition&oldid=1071834463`. [Online; accessed 25-May-2022]. 2022.

[20] H. Okamoto. “C-W (Carbon-Tungsten)”. In: *Journal of Phase Equilibria and Diffusion 2008 29:6* 29 (6 Oct. 2008), pp. 543–544. ISSN: 1863-7345. DOI: `10.1007/S11669-008-9396-7`. URL: `https://link.springer.com/article/10.1007/s11669-008-9396-7`.

[21] C. A. Campos-Roldán, R. G. González-Huerta, and N. Alonso-Vante. “Experimental Protocol for HOR and ORR in Alkaline Electrochemical Measurements”. In: *Journal of The Electrochemical Society* 165 (15 July 2018), J3001–J3007. ISSN: 0013-4651. DOI: `10.1149/2.0011815JES/XML`. URL: `https://iopscience.iop.org/article/10.1149/2.0011815jes%20https://iopscience.iop.org/article/10.1149/2.0011815jes/meta`.

[22] BioLogic. “Getting Started with EC-Lab: EIS: Electrochemical Impedance Spectroscopy”. In: ().

[23] N Murer and J.-P Diard. “Introduction to EIS (Electrochemical Impedance Spectroscopy) with EC-Lab /EC-Lab Express”. In: ().

[24] BioLogic. “Getting Started with EC-Lab: CV: Cyclic Voltammetry”. In: ().

[25] BioLogic. *EC-Lab - Software: Techniques and Applications.*

[26] Ningqiang Zhang et al. “High Pt utilization efficiency of electrocatalysts for oxygen reduction reaction in alkaline media”. In: *Catalysis Today* 332 (July 2019), pp. 101–108. ISSN: 0920-5861. DOI: `10.1016/J.CATTOD.2018.07.018`.

DEPARTMENT OF PHYSICS
CHALMERS UNIVERSITY OF TECHNOLOGY
Gothenburg, Sweden
www.chalmers.se

CHALMERS
UNIVERSITY OF TECHNOLOGY